How do earthquakes stop? Insights from a minimal model of frictional rupture

Fabian Barras[1], Kjetil Thøgersen[1], Einat Aharonov[2], and François Renard[1]

[1]University of Oslo
[2]Hebrew University of Jerusalem

December 7, 2022

Abstract

The question "what arrests an earthquake rupture?" sits at the heart of any potential prediction of earthquake magnitude. Here, we use a one-dimensional, thin-elastic-strip, minimal model, to illuminate the basic physical parameters that control the arrest of large ruptures. The generic formulation of the model allows for wrapping various earthquake arrest scenarios into the variations of two dimensionless variables $\bar \tau_k$ (initial pre-stress on the fault) and $\bar d_c$ (fracture energy), valid for both in-plane and antiplane shear loading. Our continuum model is equivalent to the standard Burridge-Knopoff model, with an added characteristic length scale, H, that corresponds to either the thickness of the damage zone for strike-slip faults or to the thickness of the downward moving plate for subduction settings. We simulate the propagation and arrest of frictional ruptures and derive closed-form expressions to predict rupture arrest under different conditions. Our generic model illuminates the different energy budget that mediates crack- and pulse-like rupture propagation and arrest. It provides additional predictions such as generic stable pulse-like rupture solutions, stress drop independence of the rupture size, the existence of back-propagating fronts, and predicts that asymmetric slip profiles arise under certain pre-stress conditions. These diverse features occur also in natural earthquakes, and the fact that they can all be predicted by a single minimal framework is encouraging and pave the way for future developments of this model.

How do earthquakes stop? Insights from a minimal model of frictional rupture

Fabian Barras[1], Kjetil Thøgersen[1], Einat Aharonov[1,2], François Renard[1,3]

[1]The Njord Centre, Departments of Geosciences and Physics, box 1048, University of Oslo, Blindern, 0316 Oslo, Norway

[2]Institute of Earth Sciences, The Hebrew University, Jerusalem, 91904, Israel

[3]ISTerre, Univ. Grenoble Alpes, Grenoble INP, Univ. Savoie Mont Blanc, CNRS, IRD, Univ. Gustave Eiffel, 38000, Grenoble, France

Key Points:

- A minimal model of frictional rupture describes large earthquake ruptures
- Two dimensionless parameters, $\bar{\tau}_k$ and $\bar{d}_c$, account for all known mechanisms of earthquake arrest
- The model illuminates the different energy balance that drives crack-like and pulse-like ruptures
- The model produces asymmetric fault slip profiles, stress drop independence of the rupture size, and back-propagating ruptures

Corresponding author: Fabian Barras, `fabian.barras@mn.uio.no`

Abstract

The question "what arrests an earthquake rupture?" sits at the heart of any potential prediction of earthquake magnitude. Here, we use a one-dimensional, thin-elastic-strip, minimal model, to illuminate the basic physical parameters that control the arrest of large ruptures. The generic formulation of the model allows for wrapping various earthquake arrest scenarios into the variations of two dimensionless variables $\bar{\tau}_k$ (initial pre-stress on the fault) and $\bar{d}_c$ (fracture energy), valid for both in-plane and antiplane shear loading. Our continuum model is equivalent to the standard Burridge-Knopoff model, with an added characteristic length scale, H, that corresponds to either the thickness of the damage zone for strike-slip faults or to the thickness of the downward moving plate for subduction settings. We simulate the propagation and arrest of frictional ruptures and derive closed-form expressions to predict rupture arrest under different conditions. Our generic model illuminates the different energy budget that mediates crack- and pulse-like rupture propagation and arrest. It provides additional predictions such as generic stable pulse-like rupture solutions, stress drop independence of the rupture size, the existence of back-propagating fronts, and predicts that asymmetric slip profiles arise under certain pre-stress conditions. These diverse features occur also in natural earthquakes, and the fact that they can all be predicted by a single minimal framework is encouraging and pave the way for future developments of this model.

Plain Language Summary

Untangling the dynamics that governs the propagation and arrest of earthquakes is still challenging, mainly because of the few constraints available on the fault zone geometry, the constitutive properties of fault materials, as well as fault rheology during the rupture event. The present study aims at formulating a model containing a minimal number of free parameters to describe the dynamics of large earthquakes. Despite its simplicity, this minimal model is able to reproduce several salient features of natural earthquakes that are still debated (e.g. various arrest scenarios, stable pulse-like rupture, back-propagating front, asymmetric slip profiles). We demonstrate how the proposed model can be used to simulate the propagation and arrest of large earthquakes, which are controlled by local variations of shear stress and material properties on the fault. With this simple and generic description, the proposed model could be readily extended to account for additional processes controlling the dynamics of large earthquakes.

1 Introduction

Frictional rupture, the process by which a dynamic rupture propagates along a pre-existing interface, has been proposed to control many geological processes, including earthquakes, landslides, glacier instabilities, and snow avalanches (e.g., Palmer and Rice (1973); Scholz (1998); Viesca and Rice (2012); Gabriel et al. (2012); Scholz (2019); Thøgersen, Gilbert, et al. (2019); Weng and Ampuero (2019); Agliardi et al. (2020); Trottet et al. (2022)). In these systems, a rupture nucleates at a given location along an interface, accelerates to a maximum velocity, and then decelerates until final arrest. The entire process is controlled by heterogeneities of the initial (normal and shear) stress conditions, roughness of the interface, and material properties along the interface and in the surrounding volume.

During frictional rupture, initial elastic strain energy stored in the volume around the interface is transformed into several components that involve 1) a transfer of elastic strain energy between different locations along the interface and in the volume around it; 2) near-fault dissipation accounting for co-seismic fracture and damage of the rock as well as frictional dissipation and heat production during slip; 3) emission of elastic waves (i.e. seismicity).

The arrest of frictional rupture can be predicted at the scale of laboratory experiments when rupture arises along the interface between two elastic blocks pressed in frictional contact (e.g. Kammer et al. (2015); Bayart et al. (2016); Ke et al. (2018)). In this setup, the prediction builds upon the analogy to brittle shear fracture and requires to know an equivalent fracture energy of the frictional plane, which varies with the normal stress. Upscaling these predictions to natural earthquakes remains out of reach due to the complexity of the fault geometry (e.g., roughness, bends, segmentation), of the fault zone rheology (e.g. damage zone), as well as due to the difficulty in estimating and measuring how the various components of the earthquake energy budget interplay in transforming and consuming the initial elastic strain energy available before rupture propagation (e.g., Abercrombie and Rice (2005); Tinti et al. (2005); Barras et al. (2020); Lambert and Lapusta (2020); Brener and Bouchbinder (2021); Paglialunga et al. (2021); Ke et al. (2022)). Prediction of rupture arrest is made even more difficult by the fact that earthquake propagation can arise under two distinct rupture modes; either crack-like or pulse-like (e.g., Scholz (2019); Lambert et al. (2021)). In conventional crack-like ruptures, also called circular cracks, all points within the growing ruptured area keep sliding until arrest (Burridge & Halliday, 1971; Madariaga, 1976; Kostrov & Das, 1988). Conversely, for pulse-like ruptures, a rupture front propagates along the interface and heals behind it, such that every point of the interface will accelerate, slip and arrest at different times (Heaton, 1990).

This complexity explains why a full comprehensive description of the conditions governing the arrest of an earthquake, and therefore its final size and magnitude, is still missing. Several scenarios of rupture arrest have been proposed in the literature and could be divided into two main categories. On the one hand, a rupture may stop because a local geometrical or mechanical heterogeneity, also called barrier, prevents further propagation (Das & Aki, 1977; Aki, 1979). On natural faults, a barrier could be related to fault segmentation (Sibson, 1985; Sibson & Das, 1986; Wesnousky, 1988; Harris & Day, 1999), to the fact that, near fault tip, rocks may be stronger and require more energy to break (e.g. concept of fault maturity, see Perrin et al. (2016)), or to variations in frictional properties (Marone & Scholz, 1988). On the other hand, a rupture may stop because of a non-local effect related to the preexisting stress along the sliding interface. For example, if a fault has been unloaded by a previous earthquake, the shear stress along the interface will be lower than for a fault that has not broken for a long period and that has been loaded by tectonic stress during that period. In this situation, a frictional rupture may arrest because of the depletion of available elastic strain energy along a section of the fault. In other words, the rupture stops because it "runs out of steam".

Here, we explore the dynamics governing the propagation and arrest of frictional rupture by using a one-dimensional elastodynamic model that contains only two parameters in its dimensionless form (Thøgersen et al., 2021). A similar approach reproduces some observations made on slow, subshear, and supershear earthquakes, such as the scaling between duration and moment (Thøgersen, Sveinsson, et al., 2019). This minimal model builds on the approximation of the earthquake dynamics existing at the later stage of the rupture once its size exceeds the width of the seismogenic zone. The resulting one-dimensional formulation, summarized in Section 2, considers a thin elastic strip in frictional contact along a preexisting interface (Fig. 1c), which may represent either a subduction setting (Fig. 1a) or a strike-slip fault (Fig. 1b) once the earthquake dynamics transition from *circular crack growth* towards the propagation of a *planar front*. Such transition is depicted by the successive dashed red lines in Fig. 1a-b and have been reported in numerical simulations (Weng & Ampuero, 2019; Day, 1982), as well as from seismic inversion of natural earthquakes (Chen et al., 2022, 2020). The elastic strip is defined by its thickness, H, and two elastic parameters, the first and second Lamé coefficients, λ and $\mathcal{G}$. H may represent the plate thickness (Fig. 1a) or the thickness of the damage zone (Fig. 1b).

The model includes inertial effects in the direction of rupture propagation but neglects them in the normal direction. Along the interface, sliding occurs according to a friction law that either considers a sharp drop from static to dynamic friction (Amontons-Coulomb model) or accounts for a weakening distance and associated fracture energy (slip-weakening model). Rupture arrest is studied and discussed for these two friction models and two different rupture modes, crack versus pulse. Our approach is both numerical (Section 3) and analytical, since the simplicity of our model allows for the reproduction of a wide range of rupture arrest scenarios and their description with analytical expressions (Section 4). Section 4 compares our one-dimensional continuum model with the seminal discrete Burridge-Knopoff model for earthquakes (Burridge & Knopoff, 1967). Using our minimal model, we present the boundary conditions that control the selection of the rupture mode (either pulse-like or crack-like) and describe the substantial difference that exists between these two modes in terms of the rupture energy balance and arrest conditions. The study concludes by highlighting how our one-dimensional framework bridges different earthquake models proposed in the literature and by discussing its implications for earthquake arrest in natural fault zones (Section 5).

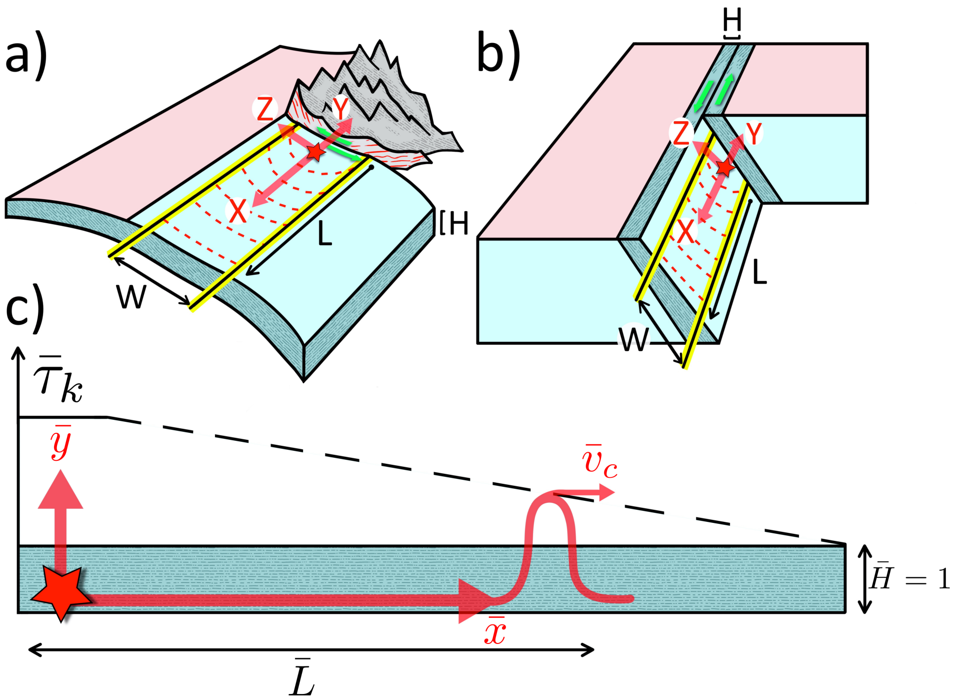

Figure 1. A minimal model to study frictional rupture arising along two types of plate boundaries, where loading is applied at a distance H from the fault. a) convergent (subduction zone or continental collision, H is the thickness of the down-moving plate), and b) transform fault (strike-slip, H is the thickness of the damage zone). In panels a) and b), the direction of plate motion is shown by a pair of green arrows. Cross-sections reveal the frictional interface between the two tectonic plates as well as the seismogenic zone of width W that hosts dynamic ruptures. Earthquake propagation is depicted by the successive red dashed lines, starting from the nucleation location shown by the red stars, and L is the rupture length. Initially, the earthquake grows as a *circular crack*. As the size of the rupture exceeds H and W, the earthquake propagates as a *planar front*. The profile of pre-stress, $\bar{\tau}_k$, is sketched in panel c) and has its peak in the nucleation zone set on the left of the domain. The propagation and arrest conditions are investigated in this study as the rupture propagates (rightwards) into a region less favorable to slip (lower pre-stress, higher frictional dissipation, barriers).

2 A one-dimensional minimal model of frictional rupture

The present study investigates rupture arrest using a minimal frictional rupture model that we developed in a previous study (Thøgersen et al., 2021). In this approach, the elastodynamic equations are reduced to a one-dimensional expression by assuming a block of finite height H in frictional contact along the plane $y = 0$, as presented in Figs. 1c and 2. The elastic fields are further taken constant along the z direction ($\partial_z u_i = 0$) during frictional ruptures that propagate along the x direction. Assuming that the rupture size L is always much larger than the system height ($L \gg H$), the elastodynamics can be solved in average over H to reduce momentum conservation into a one dimensional equation (Supplementary Information text S.1). The resulting one-dimensional equation is expressed here in dimensionless units of space $\bar{x}$ and time $\bar{t}$, with the dot accent denoting a time derivative:

$$\ddot{\bar{u}} = \frac{\partial^2 \bar{u}}{\partial \bar{x}^2} - \Gamma \bar{\gamma} \bar{u} + \bar{\tau}. \tag{1}$$

Γ is a binary operator being respectively equal to one if Eq. (1) describes a system with imposed-displacement boundary conditions at the top surface ($y = H$), or to zero if the system has imposed-stress at the top boundary. In the equation above, $\bar{u}(\bar{x}, \bar{t})$ is a scalar dimensionless displacement along the x-direction and $\bar{\tau}(\bar{x}, \bar{t})$ is a scalar dimensionless shear stress along the interface and defined as

$$\bar{\tau}(\bar{x}, \bar{t}) = \frac{\tau_0(\bar{x}) - \tau_f(\bar{x}, \bar{t})}{\sigma_n(\mu_s - \mu_k)}. \tag{2}$$

Here, $\bar{\tau}(\bar{x}, \bar{t})$ lumps the initial shear stress acting on the top of the block before the rupture τ_0, the frictional stress at the interface τ_f, the normal stress σ_n, the static μ_s and kinematic μ_k friction coefficients. The static friction coefficient describes the magnitude of the shear stress that should be locally exceeded at the interface to initiate frictional sliding. The kinematic friction coefficient describes the residual frictional stress observed at the interface during sliding. More details about the boundary conditions are given in Section S.1 of the Supporting Information. The normal stress is assumed to be constant throughout the rupture, such that the model similarly applies to elastic-over-rigid and to symmetric frictional contact problems. The momentum equation, Eq. (1), equivalently applies to in-plane (mode II) and out-of-plane (mode III) shear loading configurations, as summarized in Table S1 that compiles the definitions of the dimensionless variables.

In its simplest form, the model contains only two free parameters: 1) a dimensionless ratio of elastic moduli $\bar{\gamma}$ defined in Table S1, and 2) a spatial variable referred to as the dimensionless pre-stress in the manuscript

$$\bar{\tau}_k(\bar{x}) = \frac{\tau_0(\bar{x})/\sigma_n - \mu_k}{\mu_s - \mu_k}, \tag{3}$$

which corresponds to the value of $\bar{\tau}$ that will be observed once the frictional stress at the interface reaches kinetic friction associated to positive slip velocity. The definition of $\bar{\tau}_k$ allows for lumping spatial variations of initial stress and frictional parameters into a single variable. In the present study, we assume that variations of $\bar{\tau}_k$ results only from τ_0, but spatial variations of the other parameters (σ_n, μ_s, μ_k) can similarly be translated into a $\bar{\tau}_k(\bar{x})$ profile in the one-dimensional model with no loss of generality.

In the dimensionless form used in the model, static friction is observed as long as

$$\bar{\tau}_f(\bar{x}, \bar{t}) = \bar{\tau}_k(\bar{x}) - \bar{\tau}(\bar{x}, \bar{t}) < 1, \tag{4}$$

where $\bar{\tau}_f$ is the dimensionless frictional stress, as detailed in the section S.1, Eq. (S.13). Upon the onset of sliding, the frictional stress $\bar{\tau}_f(\bar{x}, \bar{t})$ locally drops from the static threshold ($\bar{\tau}_f = 1$) to residual friction ($\bar{\tau}_f = 0$) following the trajectory prescribed by a friction law. In the remainder of the study, we focus on two generic friction laws and we refer to Section 5 below for further discussions on how to relate more sophisticated friction laws to this minimal description. The simplest friction law assumes that the transition between static and kinematic friction is instantaneous upon sliding and requires no additional parameter. In the rest of the study, it is referred to as *Amontons-Coulomb* friction. Moreover, frictional weakening often comes with an energy dissipation on top of residual friction that will be referred to as *breakdown work*, $\bar{W}_b$. A common and generic description of this process assumes that frictional weakening between μ_s and μ_k develops linearly with slip between $\bar{u} = 0$ and some critical slip distance $\bar{u} = \bar{d}_c$. This friction law will be referred to as *slip-weakening* in the manuscript and introduces a third free parameter $\bar{d}_c$, which directly relates to the interface *fracture energy* $\bar{G}_c = \bar{d}_c/2$. $\bar{G}_c$ corresponds to the total amount of breakdown work required to reach residual friction. See section S.1 and equation (S.13) for more details on the non-dimensional descriptions of Amontons-Coulomb and slip-weakening friction laws used in this paper.

2.1 The crucial role of boundary conditions on the rupture style

Following the definitions above, $\bar{\tau}_k$ corresponds to the value of $\bar{\tau}$ in Eq. (1) observed once the shear stress (or friction) at the interface reaches its residual level. Postulating a steady-state solution and Amontons-Coulomb friction, Eq. (1) reduces to the following ordinary differential equation within the rupture (i.e. within the sliding portion of the interface):

$$(\bar{v}_c^2 - 1)\frac{\partial^2 \bar{u}}{\partial \bar{\xi}^2} = -\Gamma\bar{\gamma}\bar{u}(\xi) + \bar{\tau}_k(\xi), \tag{5}$$

with $\bar{\xi} = \bar{x} - \bar{v}_c\bar{t}$ being a co-moving coordinate following the rupture (i.e. the position of peak velocity) that moves at the propagation velocity $\bar{v}_c$.

Thøgersen et al. (2021) investigated steady-state rupture solutions governed by Eq. (5) and revealed the crucial role of boundary conditions on the rupture style and its stability. For imposed-stress boundary condition ($\Gamma = 0$), the system promotes crack-like rupture and no steady-state pulse solution exists. Pulse-like rupture can be produced under the specific condition ($\bar{\tau}_k = 0$), which reduces Eq. (5) to a one-dimensional wave equation. Such pulse solutions have no specific shape and are unstable, as a local perturbation in the stress or interface conditions $\delta\bar{\tau}_k$ either stops the pulse (if $\delta\bar{\tau}_k < 0$) or expands it into a crack (if $\delta\bar{\tau}_k > 0$). Such unstable dynamics is reminiscent of the behavior of pulse-like ruptures between two semi-infinite elastic solids that have been reported in the literature for different type of friction laws (Gabriel et al., 2012; Brener et al., 2018; Brantut et al., 2019).

Conversely, imposed-displacement boundary condition ($\Gamma = 1$) enables stable pulse solutions for $\bar{\tau}_k > 0$. Under uniform pre-stress conditions, the equation (5) allows a steady-state pulse solution with width $\bar{\omega}$ and the following slip profile:

$$\bar{u}(\bar{\xi}) = \frac{\bar{\tau}_k}{\bar{\gamma}}\Big(1 - \sin(\pi\bar{\xi}/\bar{\omega})\Big), \tag{6}$$

for $\bar{\xi} \in [-\bar{\omega}/2, \bar{\omega}/2]$. From the equation above, the final slip, $\bar{u}_p$, reached behind the steady-state pulse rupture corresponds to:

$$\bar{u}_p = 2\bar{\tau}_k/\bar{\gamma}. \tag{7}$$

Remarkably, this behavior is also in agreement with the stable pulse-like rupture that was reported in previous works studying finite elastic domains, where reflected elastic waves at the boundary interplay with the propagating rupture. This includes fault system with a damage zone with more compliant elastic properties (Idini & Ampuero, 2020) or earthquake rupture with a large aspect ratio (Weng & Ampuero, 2019). Interestingly, train of stable steady-state pulses can be produced also at the interface between unbounded elastic domains if an average slip velocity is imposed along the frictional plane instead of controlling the far-field stress (Roch et al., 2022). In our model, this second type of boundary condition ($\Gamma = 1$) corresponds then to large earthquake rupture, whose size saturates two representative dimensions of the fault systems, as depicted in Fig. 1. Thøgersen et al. (2021) discusses in details the properties of slip pulses in our one-dimensional model.

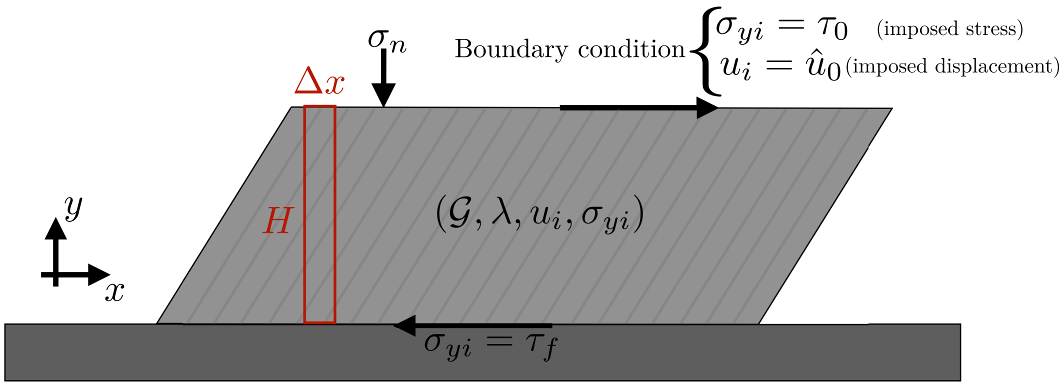

Figure 2. Sketch of the two-dimensional system that is integrated to obtain the one-dimensional equation of motion used in the manuscript. We model a thin elastic layer of thickness H with shear modulus $\mathcal{G}$ and the first Lamé coefficient λ. Two boundary conditions are considered on the top surface. At $y = H$ we apply either an imposed stress τ_0 or an imposed displacement $\hat{u}_0$. At $y = 0$, we apply a friction law. The system is integrated across the y-coordinate (red rectangle) to obtain a one-dimensional approximation. Modified from Thøgersen et al. (2021).

2.2 The arrest of frictional rupture in the one-dimensional model

The one-dimensional model (Eq. 1) used in the present study contains two free parameters for Amontons-Coulomb friction ($\bar{\gamma}$, $\bar{\tau}_k$) and an additional third parameter ($\bar{d}_c$) for slip-weakening friction. $\bar{\gamma}$ characterizes the elastic properties of the medium that are assumed to be macroscopically homogeneous and remain constant in the derivation of the model. Hence, a propagating rupture in the one-dimensional model can either be arrested by variations of $\bar{\tau}_k$ or $\bar{d}_c$. The former accounts for the level of shear stress existing in the system prior the rupture. A sharp reduction of $\bar{\tau}_k$ can stop a propagating rupture and corresponds to a *stress barrier*. Moreover, the initial finite amount of strain energy available in the surrounding bulk of thickness H scales as the square of τ_0 and is therefore proportional to $\bar{\tau}_k$. In the one-dimensional system, $\bar{\tau}_k$ describes the difference between external shear stress and the lowest value of frictional stress during sliding. If $\bar{\tau}_k$ is negative, this implies that the work injected by the external shear stress would be locally smaller than the frictional dissipation at residual frictional and, therefore, a frictional rupture would absorb energy instead of releasing it. Hence, frictional ruptures in our one-dimensional model are energetically admissible only if somewhere along the interface

$$\bar{\tau}_k \geq 0. \tag{8}$$

Note that Eq. (8) is a necessary condition for frictional rupture in the one-dimensional model but is not sufficient. It only guarantees rupture propagation once it has been nucleated. A gradual decay of $\bar{\tau}_k$ as one moves away from the nucleation site can then lead to the rupture arrest by a *depletion of available energy* in the system. Conversely, $\bar{d}_c$ describes the energy required to transform the interface shear conditions from static to kinematic friction. An increase in $\bar{d}_c$ can then arrest the rupture, which corresponds to a *fracture energy barrier*. In the Sections 3 and 4, we simulate and study theoretically pulse- and crack-like rupture arrest for these different arrest scenarios. Further in Section 5, we discuss how variations of physical conditions along natural fault systems can be expressed in terms of spatial variations of $\bar{\tau}_k$ and $\bar{d}_c$.

3 Numerical simulations of frictional rupture arrest

Here, Eq. (1) is solved numerically using a finite difference scheme with uniform grid size $\Delta\bar{x}$ and Euler-Cromer (Cromer, 1981) time-integration scheme with time step $\Delta\bar{t}$, as described in Thøgersen et al. (2021). At each grid point i and time step, the interface can be either stuck ($\dot{\bar{u}}_i = 0$) or slipping ($\dot{\bar{u}}_i \neq 0$). Static equilibrium in the stuck region, i.e. Eq. (1) with $\ddot{\bar{u}} = 0$, leads in combination with the criterion of Eq. (4) to the following inequality

$$\frac{\bar{u}_{i+1} - 2\bar{u}_i + \bar{u}_{i-1}}{(\Delta\bar{x})^2} - \Gamma\bar{\gamma}\bar{u}_i + \bar{\tau}_{k,i} < 1. \tag{9}$$

Conversely, the dynamics of the sliding portions of the interface is integrated from Eq. (1) as:

$$\ddot{\bar{u}}_i = \frac{\bar{u}_{i+1} - 2\bar{u}_i + \bar{u}_{i-1}}{(\Delta\bar{x})^2} - \Gamma\bar{\gamma}\bar{u}_i + \bar{\tau}_i + \bar{\beta}\frac{\dot{\bar{u}}_{i+1} - 2\dot{\bar{u}}_i + \dot{\bar{u}}_{i-1}}{(\Delta\bar{x})^2}, \tag{10}$$

where the scalar $\bar{\beta}$ is a small numerical parameter used to damp spurious high-frequency oscillations and is set to the standard value of $\beta = \sqrt{0.1}\Delta x$ (Knopoff & Ni, 2001; Amundsen et al., 2012). The set of equations (9)-(10) is closed by the friction law that describes the evolution of $\bar{\tau}_i$ according to Eq. (S.13). More details about the convergence and parameters of the numerical scheme are provided in the Supplementary Information, section S.2.

The initial condition of every simulation corresponds to an interface entirely stuck under a given initial shear stress defined by $\bar{\tau}_k(\bar{x})$. The domain has a finite length $\bar{\mathcal{L}}$ and the boundary conditions on the left and the right edges correspond to $\bar{u}(0) = 0$ and $\bar{u}(\bar{\mathcal{L}}) = 0$. In this study, we focus on rupture propagating from the left to the right of the domain. Rupture nucleation is triggered by defining a region of higher shear stress at the left edges with $\bar{\tau}_k(0) = 1$. Such configuration is depicted in Fig. 1c and describes rupture nucleation beyond a barrier (as for instance in Gvirtzman and Fineberg (2021)); however other nucleation processes could be considered with no loss of generality.

Figure 3 summarizes the different arrest scenarios and the simulated frictional slip observed after a pulse-like and crack-like rupture. Because $\bar{\tau}_k$ describes the excess of shear pre-stress on top of residual friction, a sharp drop of $\bar{\tau}_k$ toward negative value corresponds to a stress barrier and is presented in Fig. 3B. Frictional weakening during rupture can also involve additional energy dissipation, which in our one-dimensional slip-weakening description corresponds to $\bar{d}_c/2$. A fracture energy barrier can then be simulated by a sharp increase in $\bar{d}_c$ above some critical value $\bar{d}_c^*$, as presented in Fig. 3C. $\bar{d}_c^*$ corresponds to the largest value of $\bar{d}_c$ that can sustain further rupture propagation and is quantitatively described in the Section 4 below. Finally, frictional ruptures can stop by running out of available energy in the system, which is function of the initial shear stress and whose depletion can be modelled by a progressive decay of $\bar{\tau}_k$, as presented in Fig. 3D.

The comparison of rupture styles in Fig. 3 sheds light on the significant difference in terms of final slip that exists between the two frictional rupture modes. Most notably, the profile of slip observed after a pulse-like rupture is much more sensitive to the arrest scenarios and keeps a precise record of the local variations of bulk and interface conditions compared to the profile of slip observed after crack-like rupture.

4 Theoretical description of the arrest of pulse- and crack-like ruptures

4.1 Equivalence to the Burridge-Knopoff approach

The one-dimensional model expressed in its discretized form in Eqs. (9) and (10) is equivalent to Burridge-Knopoff type of models widely used in the literature to describe earthquakes rupture and statistics (e.g., Burridge and Knopoff (1967); Olami et al. (1992); Carlson et al. (1994); Brown et al. (1991); Braun et al. (2009); Trømborg et al. (2014)). Starting from the seminal work of Burridge and Knopoff (1967), the Burridge-Knopoff

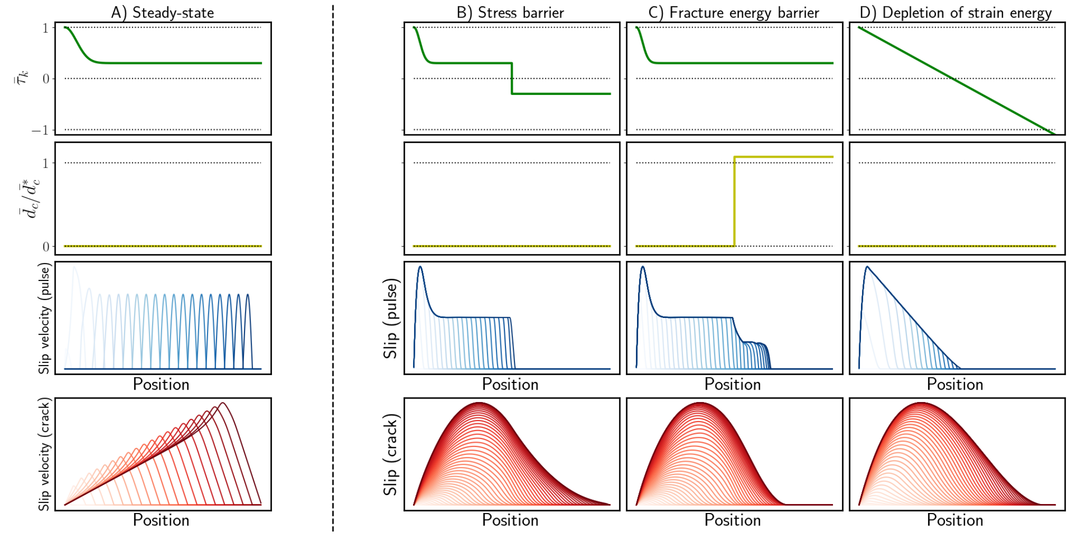

Figure 3. Slip velocities and three arrest scenarios studied in the present study with the resulting final slip profiles observed after a pulse-like (blue) and a crack-like (red) rupture. Slip velocities and slip profiles are calculated by solving numerically the Eq. (1). In each column, the top two panels display the initial profiles of pres-stress and fracture energy along the interface. Rupture is nucleated by a larger value of pre-stress located near $\bar{x} = 0$. A) Steady-state slip velocities for pulse-like and crack-like ruptures. The increasing color shade of each slip profile indicates progression in time. B) A sharp drop of $\bar{\tau}_k$ forms a stress barrier that arrests frictional rupture. C) The frictional rupture is arrested by a sharp increase in $\bar{d}_c$ that corresponds to a fracture energy barrier. D) A linear decay of $\bar{\tau}_k$ progressively reduces the available strain energy to propagate the frictional rupture and eventually arrests it.

model for earthquakes consists of a horizontal array of blocks with identical mass connected by longitudinal springs. Each block is submitted to a normal force and resists horizontal sliding by friction. The system is either loaded by applying a lateral forces or by connecting each block to a moving support via vertical springs, often referred to as leaf springs. Our one-dimensional formulation of Eq. (10) can be obtained from Burridge-Knopoff models by setting blocks mass to unity, lateral springs stiffness to $(\Delta\bar{x})^2$, and the leaf springs stiffness to $\bar{\gamma}$. This analogy is exploited later in the present study to derive pulse and crack equations inspired from Burridge-Knopoff models. Our one-dimensional model represents therefore an interesting framework to bridge the discrete description of earthquake dynamics provided in Burridge-Knopoff models to continuum models of faults. The main difference of our approach is that we introduce here a characteristic length scale H, that does not exist in Burridge-Knopoff models.

4.2 One-dimensional energy balance

The different contributions to the energy balance of the one-dimensional system correspond to the *elastic energy* $\bar{E}_{\text{el}}$, the *kinetic energy* $\bar{E}_{\text{kin}}$, and the *external work* $\bar{W}_{\text{ext}}$. During the frictional rupture, the work done by the external forces is converted into internal energy such that: $\bar{W}_{\text{ext}} = \bar{E}_{\text{el}} + \bar{E}_{\text{kin}}$. In analogy to Burridge-Knopoff models with $\mathcal{N}$ blocks, the elastic energy corresponds to the potential energy stored in the longitudinal springs and the leaf springs:

$$\bar{E}_{\text{el}} = \sum_{1}^{\mathcal{N}-1} \frac{1}{2}(\Delta\bar{x})^{-2}(\bar{u}_{i+1} - \bar{u}_i)^2 + \Gamma \sum_{1}^{\mathcal{N}} \frac{1}{2}\bar{\gamma}\bar{u}_i^2 \tag{11}$$

or in the continuum form

$$\bar{E}_{\text{el}} = \frac{1}{2}\int_0^{\bar{\mathcal{L}}} \left(\frac{\partial\bar{u}}{\partial\bar{x}}\right)^2 d\bar{x} + \Gamma\frac{1}{2}\int_0^{\bar{\mathcal{L}}} \bar{\gamma}\bar{u}^2 d\bar{x}. \tag{12}$$

Note that the second right-hand-side contribution to the elastic energy in Eq. (12) (i.e. the leaf springs in the Burridge-Knopoff model) only arises for imposed-displacement boundary condition ($\Gamma = 1$, pulses). Similarly, the kinetic energy corresponds to

$$\bar{E}_{\text{kin}} = \frac{1}{2}\int_0^{\bar{\mathcal{L}}} \left(\frac{\partial\bar{u}}{\partial\bar{t}}\right)^2 d\bar{x}. \tag{13}$$

The external work corresponds to

$$\bar{W}_{\text{ext}} = \int_0^{\bar{\mathcal{L}}} \left(\bar{\tau}_k\bar{u} - \bar{W}_b(\bar{u})\right) d\bar{x}. \tag{14}$$

From the definition of $\bar{\tau}_k$ in Eq. (3), the first term on the right-hand side of Eq. (14) combines the work of the external shear stress τ_0 and the work done against residual friction. The second right-hand side term $\bar{W}_b$ accounts for additional dissipation on top of residual friction in case of slip-weakening friction, the so-called *breakdown work*, and is given by

$$\bar{W}_b(\bar{u}) = \int_0^{\bar{u}} \bar{\tau}_f(\mathcal{U})\,\mathrm{d}\mathcal{U}, \tag{15}$$

with $\bar{\tau}_f(\bar{u})$ defined in Eq. (S.13).

It is important to note that the initial level of internal energy in the one-dimensional system is set as zero ($\bar{E}_{\text{el}} + \bar{E}_{\text{kin}} = \bar{W}_{\text{ext}} = 0$). Throughout the rupture, the variation of elastic strain energy into a three-dimensional solid of dimensions $\mathcal{L} \times H \times W$ is accounted for in the one-dimensional model by change in $\bar{W}_{\text{ext}}$ and $\bar{E}_{\text{el}}$. For the simplicity of the argument, let us assume Amontons-Coulomb friction and homogeneous slip along the horizontal extent $\bar{L}$ of a frictional rupture such that only the second right-hand-side term of Eq.(12) contributes to the elastic energy. The amount of energy released by the rupture into the system corresponds to

$$\bar{E}_r = \bar{W}_{\text{ext}} - \bar{E}_{\text{el}} = \bar{L}\Big(\bar{\tau}_k\bar{u} - \frac{1}{2}\Gamma\bar{\gamma}\bar{u}^2\Big), \tag{16}$$

which is converted into kinetic energy. Frictional rupture is *energetically admissible* if $\bar{E}_r \geq 0$.

For imposed-stress boundary conditions ($\Gamma = 0$), frictional slip is admissible as long as $\bar{\tau}_k \geq 0$, and the larger the slip the more energy is released in the system. Conversely, for imposed-displacement boundary conditions ($\Gamma = 1$), part of the work injected by the pre-stress in the system goes into the leaf spring elastic energy, such that frictional slip is only admissible for $0 \leq \bar{u} \leq 2\bar{\tau}_k/\bar{\gamma}$, with the upper bound being equivalent to the steady-state slip solution of Eq. (7). This different energy transfer between stress- and displacement-controlled conditions explains why, in the wake of the propagating rupture, the interface re-stick (i.e pulse-like rupture) for $\Gamma = 1$ whereas sliding continues in the form of a crack-like rupture for $\Gamma = 0$. Physically, this one-dimensional energy balance describes the fact that the shear stress τ_0 remains constant in the three-dimensional solid during the rupture for imposed-stress boundary conditions, whereas τ_0 progressively drops with frictional slip if the displacement is imposed at the top surface of the block, according to Figure 2. In the Supplementary Information sections S.3 and S.4, this one-dimensional energy balance is exploited further to describe frictional rupture beyond the homogeneous steady-state simplification in order to propose pulse and crack arrest equations which are summarized hereafter.

4.3 Pulse arrest equations

First, we follow the approach proposed by Elbanna and Heaton (2012) and derive a pulse equation by integrating the energy balance between the nucleation site $\bar{x} = 0$ to the leading tip of the pulse $\bar{x} = \bar{L}$. Next, we assume that the ruptured area is larger than the width of the pulse $\bar{L} \gg \bar{\omega}$ to neglect the contribution of the regions within the pulse width and obtain the following ordinary differential equation:

$$\frac{\partial^2 \bar{u}_p}{\partial \bar{x}^2} = \bar{\gamma}\bar{u}_p - 2\bar{\tau}_k + \frac{2\bar{W}_b(\bar{u}_p)}{\bar{u}_p}, \tag{17}$$

with $\bar{u}_p$ being the final slip reached in the wake of the traveling pulse. The detailed derivation of Eq. (17) can be found in the section S.3.

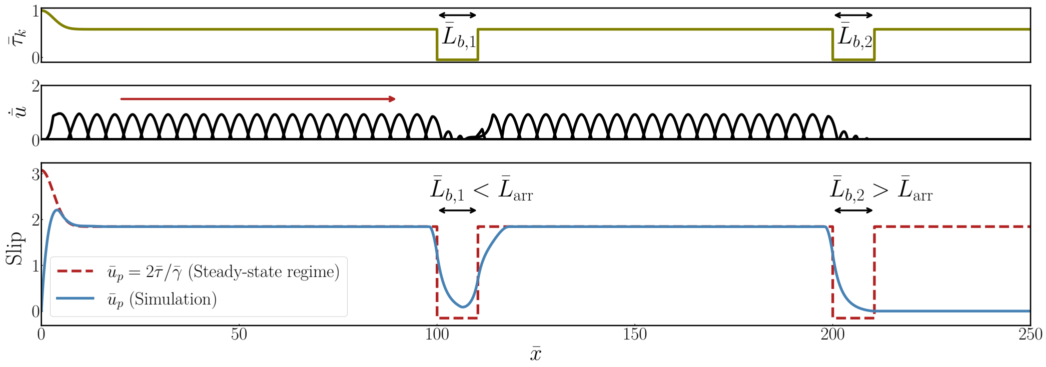

Figure 4. Example of slip pulse simulation. *Top*: Profile of the initial pre-stress, $\bar{\tau}_k$, with a Gaussian stress concentration introduced on the left side of the domain to nucleate frictional rupture. Stress barriers with similar amplitude $\bar{\tau}_{k,b} = -10^{-4}$ but various lengths $\bar{L}_{b,i}$ are placed along the fault at $\bar{x} = 100$ and $\bar{x} = 200$. *Middle*: Snapshots of slip velocity at different time steps, showing slip pulse propagation in the direction of the red arrow. Note that the pulse crossed the first barrier, but was stopped by the longer second barrier. *Bottom*: Final slip profile compared to the steady-state regime. A propagating pulse can cross a barrier of length smaller than the arrest length $\bar{L}_{\text{arr}}$ but is arrested by a barrier that is larger than $\bar{L}_{\text{arr}}$

.

4.3.1 Stress barriers

This arrest scenario is studied by simulating a steadily propagating pulse under a given initial stress $\bar{\tau}_{k,0}$ that reaches a region of lower pre-stress at $\bar{x} = \bar{x}_b$, as shown in Fig. 4. If the shear stress within the barrier $\bar{\tau}_{k,b}$ is still positive, a steady-state pulse solution exists and the final slip evolves toward the new steady-state according to Eq. (7). If $\bar{\tau}_{k,b}$ is negative (as in Fig 4), sustained pulse propagation is no longer possible such that the rupture will be arrested for barriers that exceed a critical length defined as $\bar{L}_{\text{arr}}$. The pulse equation (17) can be used to predict the decay of slip observed in Fig. 4 within a barrier of negative pre-stress. For negligible breakdown work (i.e. Amontons-Coulomb friction with $\bar{W}_b = 0$), the general solution of Eq. (17) is the sum of two exponential functions. As shown in Figure S2, the pulse arrest equation Eq. (17) can be used to derive different predictions of the decay of frictional slip within the barrier from its initial steady-state value $u_p = 2\bar{\tau}_k/\bar{\gamma}$. For instance, the following solution is obtained by searching for solution where both $\bar{u}_p(\bar{x}')$ and its first derivative are equal to zero at the arrest location:

$$\bar{u}_p(\bar{x}') = \frac{-2\bar{\tau}_{k,b}}{\bar{\gamma}}\Big(\cosh\Big((\bar{x}' - \bar{L}_{\text{arr}})\sqrt{\bar{\gamma}}\Big) - 1\Big), \tag{18}$$

with $\bar{x}' = \bar{x} - \bar{x}_b$, where x_b is the position at which the barrier starts. Remembering that $\bar{\tau}_{k,b} < 0$, the equation above has a positive root $\bar{u}_p(\bar{x}' = \bar{L}_{\text{arr}}) = 0$ which can be used to predict the arrest length:

$$\bar{L}_{\text{arr}} = \bar{\gamma}^{-\frac{1}{2}}\text{arccosh}\Big(\frac{\bar{\tau}_{k,0} - \bar{\tau}_{k,b}}{-\bar{\tau}_{k,b}}\Big). \tag{19}$$

Figure 5(A) compares this theoretical prediction with the numerical simulations for various stress barriers ($-\bar{\tau}_{k,b}$) with different initial prestress ($\bar{\tau}_{k,0}$) and moduli $\bar{\gamma}$. The theoretical prediction of Eq. (19) captures well the trend observed in the simulations but systematically underestimates the simulated arrest length. This underestimation comes from the simplification behind the pulse arrest equation (17), which neglects the finite width of the pulse and associated mechanical energy. As shown in Figure S2, frictional slip in the simulations starts decaying before the barrier location due to the finite width of the pulse.

4.3.2 Fracture energy barriers

If the contribution of the breakdown energy is non-negligible (slip-weakening friction), two end-member situations can occur. In a first case, frictional weakening is complete in the wake of the rupture, such that the breakdown work is constant and equates the fracture energy prescribed in the slip weakening friction law, $\bar{W}_b = \bar{G}_c = \bar{d}_c/2$. Equation (17) is a non-linear ordinary differential equation, but the possibility for smoothly travelling pulse can nevertheless be investigated by neglecting the second-order derivative, which leads to the following slip solution behind the travelling pulse:

$$\bar{u}_p = \frac{\bar{\tau}_k}{\bar{\gamma}}\Big(1 + \sqrt{1 - \frac{\bar{d}_c\bar{\gamma}}{\bar{\tau}_k^2}}\Big). \tag{20}$$

Note how Eq. (20) leads to the steady-state solution for Amontons-Coulomb friction of Eq. (7) as $\bar{d}_c \to 0$. Interestingly, neglecting the contribution of the fracture energy in the steady-state pulse solution leads to an overestimation of the final slip by at most a factor two. The solution Eq. (20) leads to the definition of a critical value of $\bar{d}_c$, above which sustained pulse propagation is no longer admissible:

$$\bar{d}_c^* = \bar{\tau}_k^2/\bar{\gamma}. \tag{21}$$

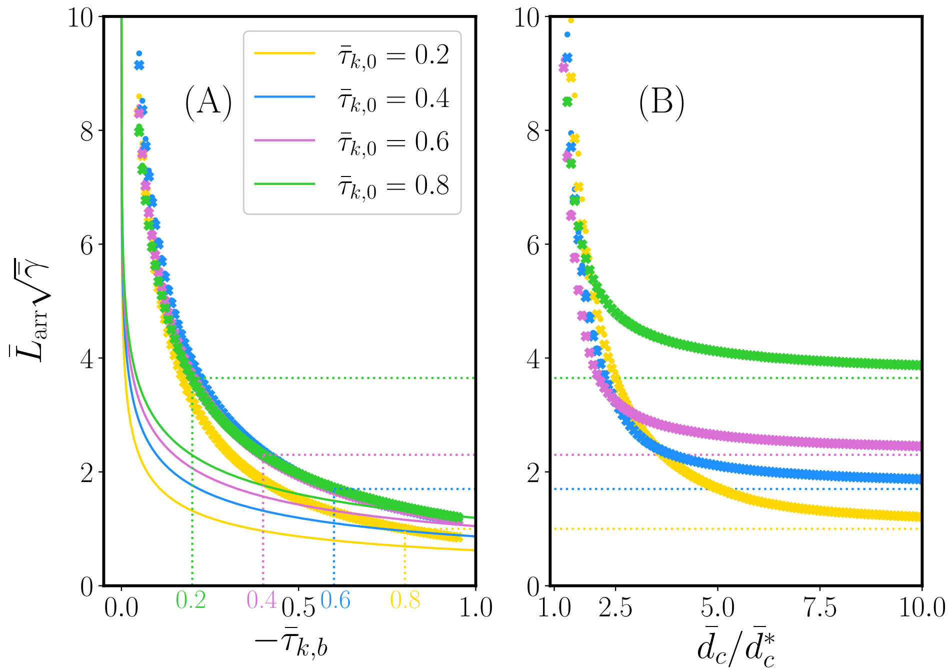

Figure 5. Arrest length for slip pulse in presence of stress (A) and fracture energy (B) barriers. The solid lines on the plot (A) correspond to the theoretical prediction given by Eq. (19). Color symbols correspond to simulation results at different initial stresses $\tau_{k,0}$ for $\bar{\gamma} = 0.65$ (circle) and $\bar{\gamma} = 2.0$ (cross). The dashed horizontal lines highlight how the stress barrier with amplitude $\bar{\tau}_{k,b} = \tau_{k,0} - 1$ gives the asymptotic value of the arrest length for tough fracture energy barriers $\bar{d}_c \gg \bar{d}_c^*$.

Using Eqs. (20), one can rewrite the pulse equation (17) and defined ð as

$$\frac{\partial^2 \bar{u}_p}{\partial \bar{x}^2} = \bar{\gamma}\bar{u}_p - 2\bar{\tau}_k + \frac{\bar{d}_c}{\bar{u}_p} = \bar{\gamma}\bar{u}_p - \bar{\tau}_k\left(2 - \frac{\bar{d}_c/\bar{d}_c^*}{1+\sqrt{1-\bar{d}_c/\bar{d}_c^*}}\right) \equiv \bar{\gamma}\bar{u}_p - ð\bar{\tau}_k, \qquad (22)$$

with $1 \leq ð \leq 2$ being a constant that depends on the interface fracture energy. For the largest admissible fracture energy ($\bar{d}_c = \bar{d}_c^*$), one has $ð = 1$, whereas for zero fracture energy $ð = 2$.

As in the case of stress barriers, a fracture energy barrier with $\bar{d}_c > \bar{d}_c^*$ will arrest the rupture if its length is larger than some arrest length $\bar{L}_{\mathrm{arr}}$. This leads to the other situation for which frictional weakening is incomplete in the wake of the rupture ($\bar{W}_b < \bar{d}_c/2$). The integration of the breakdown work according to Eq. (15) leads to the following ordinary differential equation:

$$\frac{\partial^2 \bar{u}_p}{\partial \bar{x}^2} = \left(\bar{\gamma} - \frac{1}{\bar{d}_c}\right)\bar{u}_p - 2(\bar{\tau}_k - 1). \tag{23}$$

For very large $\bar{d}_c$, the equation above is identical to the one describing a stress barrier with $\bar{\tau}_{k,b} = \bar{\tau}_k - 1$. Physically, this means that there is not enough slip and energy to drive the weakening of the interface within the barrier such that frictional stress stays close to the static value (corresponding to $\bar{\tau} = \bar{\tau}_k - 1$) throughout the width of the pulse. An important implication is that any fracture energy barrier with a length shorter than

$$\bar{L}^*_{\text{arr}} = \bar{L}_{\text{arr}}(\bar{\tau}_{k,b} = \bar{\tau}_{k,0} - 1) \tag{24}$$

cannot stop a propagating slip pulse regardless of its fracture energy amplitude. The figure 5(B) presents the two asymptotic situations that describe the arrest of pulse-like rupture by a fracture energy barrier: $\bar{L}_{\text{arr}}$ diverges as $d_c \to \bar{d}^*_c$, whereas for $d_c \to \infty$ the arrest length converges towards $\bar{L}^*_{\text{arr}}$.

4.3.3 Progressive decay of available strain energy

Ruptures can also be arrested by smoothly decaying prestress, $\bar{\tau}_k$. Indeed, earthquakes typically nucleate in a critically stressed portion of a fault before reaching subcritically stressed regions. In the one-dimensional model, stress criticality is described by the dimensionless variables $\bar{\tau}_k$ (with critical values corresponding to $\bar{\tau}_k > 1$). Pulse rupture in a smoothly decaying pre-stress can be described using the pulse arrest equation. For example with a linearized decaying profile of the form $\bar{\tau}_k(\bar{x}) = 1 - \bar{\alpha}\bar{x}$, the following final slip profile satisfies Eq. (17):

$$\bar{u}_p = \frac{2}{\bar{\gamma}}\Big(1 - \bar{\alpha}\bar{x} - \exp(-\bar{x}\sqrt{\bar{\gamma}})\Big). \tag{25}$$

Similarly, for a quadratic decay of the prestress profile of the form $\bar{\tau}_k = 1 - \bar{\lambda}\bar{x}^2$, the following profile of slip can be predicted using the pulse equation:

$$\bar{u}_p = \frac{2}{\bar{\gamma}}\Big((1 - 2\bar{\lambda}\bar{\gamma}^{-1})(1 - \exp(-\bar{x}\sqrt{\bar{\gamma}})) - \bar{\lambda}\bar{x}^2\Big). \tag{26}$$

Figure 6 validates the theoretical predictions (25) and (26) derived from the pulse equation with numerical simulations. Accounting for the contribution of the growing exponential term $\sim \exp(\bar{x}\sqrt{\bar{\gamma}})$, which was neglected in the derivation of Eqs. (25) and (26), could further improve the predicted slip closed to the arrest position.

For slowly decaying prestress (i.e., $\bar{\alpha}; \bar{\lambda} \ll 1$), both equations (25) and (26) predict that the rupture arrests at the location where $\bar{\tau}_k = 0$, which leads to $L_{\mathrm{ar}} \cong \bar{\alpha}^{-1}$ and $L_{\mathrm{ar}} \cong \bar{\lambda}^{-1/2}$, respectively for the linear and quadratic prestress. In dimensional units, the rupture is then expected to arrest where the initial shear stress τ_0 becomes smaller than residual friction $\mu_k \sigma_n$.

Remarkably, these generic decaying loading conditions produce asymmetric, triangular, slip profiles reminiscent of the slip profiles reported in natural fault zones (Manighetti et al., 2005, 2009). After nucleation, the rapid slip rise is governed by elasticity and the exponential term $(1-\exp(-\bar{x}\sqrt{\bar{\gamma}}))$. Post peak, the slow decay mimics the profile of initial stress and is governed by the linear term of Eq. (25) or the quadratic decay in Eq (26).

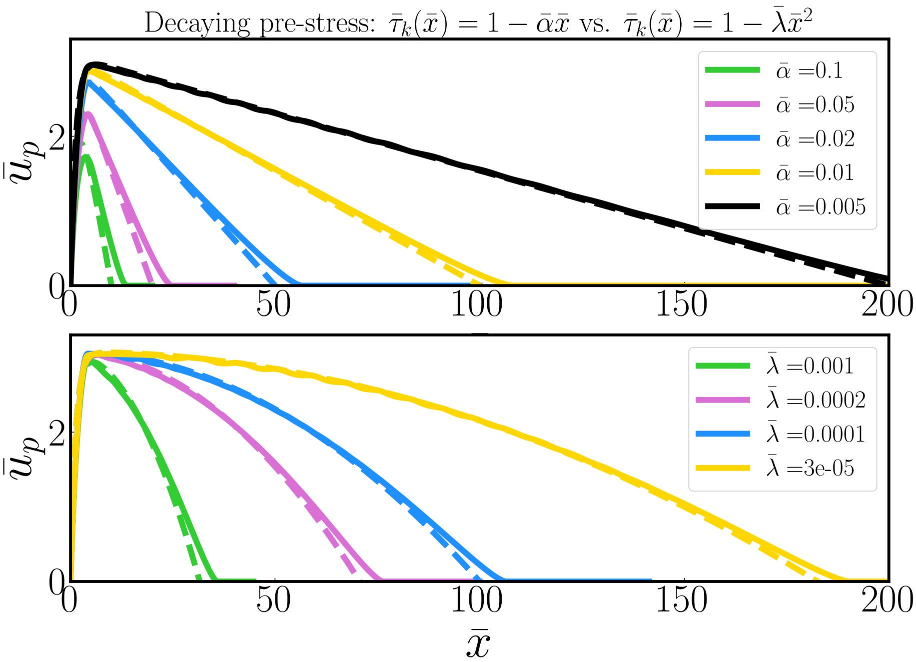

Figure 6. Profile of final slip caused by a pulse-like rupture propagating towards a region with decaying pre-stress: simulations (solid lines) versus the analytical predictions (dashed-lines) derived from the pulse arrest equation (17). Top: Linearly decaying pre-stress with final slip predicted by Eq. (25). Bottom: Quadratically decaying pre-stress with final slip predicted by Eq. (26)

4.4 Crack arrest equations

Crack-like rupture in Burridge-Knopoff models have received more attention in the literature compared to pulses. Past works (e.g. Trømborg et al. (2011); Amundsen et al. (2012)) showed that the arrest of cracks in these models can be well predicted using the net shear force acting on the sliding block just ahead of the propagating tip, which corresponds, in our one-dimensional model, to the following integral:

$$\bar{K}(\bar{L}) = \int_0^{\bar{L}} \bar{\tau}_k(\bar{x})\, \mathrm{d}\bar{x}. \tag{27}$$

Crack-like ruptures have different energy budget than pulses. First, kinetic energy during the rupture is not concentrated near the propagating tip but spreads over the entire ruptured area. Second, there is no contribution from the leaf spring elastic energy because $\Gamma = 0$ in Eq. (12). Therefore, the work done by the external stress W_{ext} is converted into strain and kinetic energy within the crack and corresponds to the energy released by the rupture.

To illustrate the difference of energy budget governing pulse and crack dynamics, we derive the steady-state solution for a propagating crack under homogeneous conditions in the section S.4.1 of the Supplementary Information. Using this steady-state solution, we can compute the energy released by the rupture, which corresponds to

$$\bar{E}_{\text{crack}} = \frac{\bar{\tau}_k^2 \bar{L}^3}{6\bar{v}_c(\bar{v}_c + 1)} \tag{28}$$

for a crack of size $\bar{L}$ propagating at speed $\bar{v}_c$. For homogeneous conditions, $K(\bar{L}) = \bar{\tau}_k \bar{L}$ can then be related to $\bar{E}_{\text{crack}}$ by expressing the rate of energy release per unit crack advance, $\bar{G}$:

$$\bar{G}(\bar{L}, \bar{v}_c) = \frac{\mathrm{d}\bar{E}_{\text{crack}}}{\mathrm{d}\bar{L}} = \frac{\bar{\tau}_k^2 \bar{L}^2}{2\bar{v}_c(\bar{v}_c + 1)} = \bar{K}^2 \bar{\mathcal{A}}(\bar{v}_c). \tag{29}$$

By analogy with dynamic fracture mechanics (e.g. Freund (1998)), $\bar{K}$ and $\bar{G}$ correspond to the one-dimensional stress intensity factor and the energy release rate, whereas $\bar{\mathcal{A}}$ is some universal function of the rupture speed.

4.4.1 Stress barriers

For a stress barrier, the arrest location of crack-like rupture is well predicted by the first position along the crack path where the net force acting on the sliding element ahead of the tip becomes zero (Trømborg et al., 2011; Amundsen et al., 2012). Using Eq. (27), the predicted arrest length $\bar{L}_{\text{arr}}$ of crack-like rupture in the one-dimensional model can be readily defined as $\bar{K}(\bar{x}_b + \bar{L}_{\text{arr}}) = 0$, which implies that

$$\bar{L}_{\text{arr}} = -\frac{\bar{x}_b \bar{\tau}_{k,0}}{\bar{\tau}_{k,b}}, \tag{30}$$

recalling that $\bar{\tau}_{k,b}$ has to be negative to form a stress barrier. Unlike pulse-like rupture (see Eq. (19)), the arrest length of crack also depends on the position of the barrier $\bar{x}_b$. This is explained by the fact that the energy released by a crack depends on its size $\bar{L}$ to a cubic power (see Eq. (28)), whereas the energy released by a steadily propagating pulse is constant and only depends on $\bar{\tau}_k$ (see Eq. S.30 and Supplementary Information section S.3.4 for more details).

4.4.2 Fracture energy barriers

As discussed in the context of pulses, the two characteristic quantities $\bar{d}_c^*$ and $\bar{L}_{\text{arr}}^*$ can be similarly defined for cracks. $\bar{d}_c^*$ corresponds to the minimal amount of fracture energy required to arrest the rupture (sustained rupture growth is admissible for $\bar{d}_c < \bar{d}_c^*$). $\bar{L}_{\text{arr}}^*$ corresponds to the minimum barrier length required to arrest the rupture (no fracture energy barrier with size $\bar{L}_{\text{arr}} < \bar{L}_{\text{arr}}^*$ can arrest a propagating rupture). The main difference is that for crack-like rupture both $\bar{d}_c^*$ and $\bar{L}_{\text{arr}}^*$ depend on the size of the crack ($\bar{L} = \bar{x}_b$).

As in the case of pulse-like rupture, $\bar{L}_{\text{arr}}^*$ corresponds to the arrest length caused by a stress barriers with $\bar{\tau}_{k,b} = \bar{\tau}_k - 1$, which leads to the following expression using (30)

$$\bar{L}_{\text{arr}}^*\Big(\bar{\tau}_k, \bar{x}_b\Big) = \frac{\bar{x}_b \bar{\tau}_k}{1 - \bar{\tau}_k}. \tag{31}$$

As discussed for pulse-like rupture, $\bar{L}_{\text{arr}}^*$ above governs rupture arrest in the asymptotic limit $\bar{d}_c \to \infty$, for which frictional weakening is limited and $\bar{\tau}_f$ stays near the static value.

The other end-member situation corresponds to fully developed frictional weakening such that $\bar{W}_b = \bar{G}_c = \bar{d}_c/2$. The one-dimensional dynamic fracture energy balance ($\bar{G} = \bar{G}_c$) can be used together with Eq. (29) to define critical fracture energy following the derivation detailed in the Supplementary Information, section S.4:

$$\bar{d}_c^*(\bar{\tau}_k, \bar{x}_b) = \left(\frac{4\bar{x}_b}{3}\right)^2 (1 - \bar{\tau}_k^2)\Big(1 - \sqrt{1 - \bar{\tau}_k^2}\Big). \tag{32}$$

Figure 7 tests the predictions of $\bar{L}_{\text{arr}}^*$ (31) and $\bar{d}_c^*$ (32) against simulations that span several orders of magnitude of fracture energy barrier and arrest length. First, it shows that the simplifications behind Eq. (32) gives an accurate prediction for moderate pre-stress.

343 At large pre-stress, dynamical effects associated to fast crack speed tend to overshoot
344 the prediction of $\bar{L}_{\mathrm{arr}}$ in Eq. (S.44) and, thereby, $\bar{d}_c^*$. Second, the arrest of crack-like rup-
345 ture is much sharper than in the case of slip pulse, such that $\bar{L}^*_{\mathrm{arr}}(\bar{x}_b)$ (31) always pro-
346 vides a good approximation of the arrest length by a fracture energy barrier.

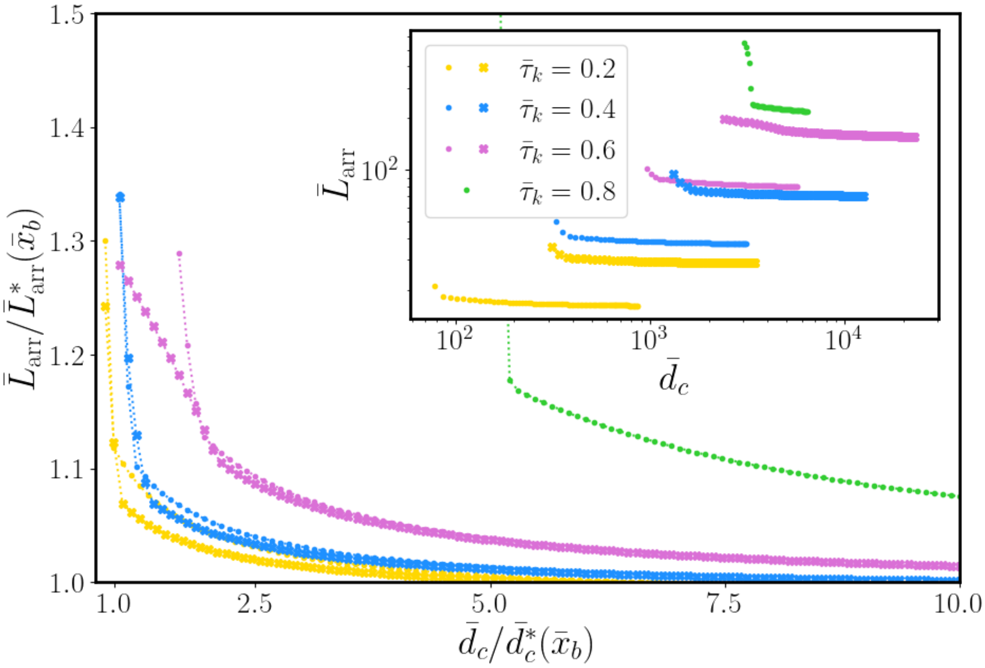

Figure 7. Arrest length of crack-like rupture stopped by a fracture energy barrier simulated for different values of initial stress $\bar{\tau}_k$ and fracture energy amplitude $\bar{d}_c$. The markers identify simulations with barrier size $\bar{x}_b = 50$ (dots) and $\bar{x}_b = 100$ (crosses). The inset shows the raw data that spans several orders of magnitude in $\bar{L}_{\mathrm{arr}}$ and $\bar{d}_c$, and that are collapsed in the main plot using the definitions of $\bar{d}_c^*$ in Eq. (32) and $\bar{L}^*_{\mathrm{arr}}$ in Eq. (31).

347 *4.4.3 Progressive decay of available energy*

348 As in the case of stress barriers, the one-dimensional stress intensity factor defined
349 in Eq. (27) can be readily used to predict the arrest of a crack-like rupture under smoothly
350 decaying pre-stress conditions as $\bar{K}(\bar{L}_{\mathrm{arr}}) = 0$. In the case of the linearly decaying shear
351 stress $\bar{\tau}_k = 1 - \bar{\alpha}\bar{x}$, the arrest length corresponds then to $\bar{L}_{\mathrm{arr}} = 2/\bar{\alpha}$ and is twice larger
352 than in the case of a pulse-like rupture. For quadratic decay of the pre-stress $\bar{\tau}_k = 1 -$
353 $\bar{\lambda}\bar{x}^2$, the arrest length corresponds then to $\bar{L}_{\mathrm{arr}} = \sqrt{3/\bar{\lambda}}$. Using this arrest prediction,

the one-dimensional energy balance can be used to derive a theoretical prediction of the profile of the final slip $\bar{u}_p$, as detailed in the Supplementary Information, section S.4.2. As shown in Figure 8, the solution allows to collapse the final slip profile simulated with different values of $\bar{\alpha}$ and $\bar{\lambda}$. Important differences exist between the slip profile after pulse-like rupture shown in Fig. 6 and the slip observed after crack-like rupture in Fig. 8. Slip profiles after pulse-like rupture record the initial variations of the prestress before the rupture, whereas crack-like rupture tends to homogenize and average local variations of prestress. Mechanically, this difference arises because crack releases energy over the entire rupture length $\bar{L}$, whereas pulse energy balance is more local and concentrated in the thin width $\bar{\omega}$ near the rupture tip. Mathematically, this difference translates into slip profile governed by a differential equation for pulses, Eq. (17), versus an integral equation that governs $\bar{u}_p$ for cracks, Eqs. (S.46)-(S.47). Consequently, when propagating towards decaying pre-stress, slip pulses produce asymmetric slip profiles, whereas crack-like ruptures produce slip profiles where the relative position of the maximum slip often lies between one third and one half of the arrest distance $\bar{L}_{\mathrm{arr}}$. Consequently, in this setup, pronounced asymmetric, triangular, slip profiles are exclusively the signature of pulse-like ruptures.

5 Discussion

5.1 Connection to existing earthquake models

The differential equation solved in our one-dimensional model can be related to the equation of motion of spring-block systems used in Burridge-Knopoff models (Burridge & Knopoff, 1967; Burridge & Halliday, 1971). This analogy is directly used in the present study to calculate the energy balance and we propose analytical predictions of the rupture dynamics. Our one-dimensional system of equations brings an additional length scale H that is missing in the classical spring-block models and allows to bridge them to the continuum elastic description of faulting. Indeed, the one-dimensional model allows for capturing several characteristics of rupture dynamics described in two- and three-dimensional models of fault under different boundary conditions.

Under imposed-stress boundary conditions ($\Gamma = 0$), ruptures simulated with the one-dimensional model have similar dynamics to that of cracks propagating in unbounded elastic domain. In such setup, the most frequent rupture mode corresponds to the propagation of a shear crack (e.g. Kostrov, 1966; Ida, 1972), whereas slip-pulses are inher-

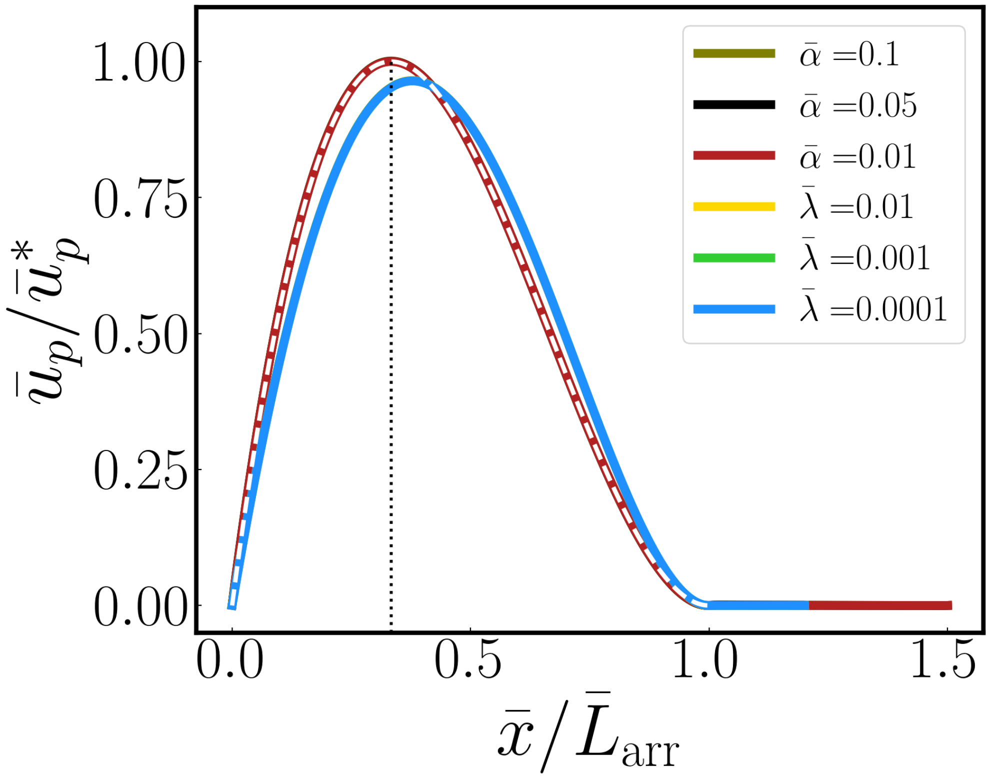

Figure 8. Simulation (solid line) versus theoretical prediction (white dashed-line) of the final slip profile observed for a crack-like rupture with a linear decay ($\bar{\tau}_k(\bar{x}) = 1 - \bar{\alpha}\bar{x}$) or a quadratic decay ($\bar{\tau}_k(\bar{x}) = 1 - \bar{\lambda}\bar{x}^2$) of the pre-stress. As derived in Supplemental Information, section S.4.2, $\bar{L}_{\rm arr}$ corresponds respectively to $\bar{\alpha}/2$ and $\sqrt{3/\bar{\lambda}}$ for the linear and quadratic decays, whereas the maximum slip $\bar{u}_p^*$ is respectively given by $4/(27\bar{\alpha}^2)$ and $2/(9\bar{\lambda})$. The position of maximum slip is most often located near $\bar{x} = \bar{L}_{\rm arr}/3$, as highlighted by the vertical black dotted line.

ently unstable and emerge under specific loading and interface conditions (Zheng & Rice, 1998; Gabriel et al., 2012; Brener et al., 2018; Brantut et al., 2019). As in the one-dimensional model under imposed-stress boundary conditions, the system supplies an unlimited amount of energy to the propagating rupture and promotes crack-like rupture whose energy release rate increases with the rupture size. The one-dimensional setup includes an additional length scale H, such that the crack energy release rate scales as $G \sim (\Delta\tau)^2\mathcal{G}^{-1}L^2H^{-1}$ instead of the scaling $G \sim (\Delta\tau)^2\mathcal{G}^{-1}L$ relevant for circular cracks in an infinite domain. Apart from this different scaling, the crack arrest criterion predicted by Eq. (27) is the one-dimensional analogue of the shear fracture criterion that was successfully used to predict the arrest of frictional rupture in laboratory experiments (Kammer et al., 2015; Bayart et al., 2016; Ke et al., 2018).

Under displacement-controlled boundary conditions ($\Gamma = 1$), the rupture dynamics is substantially different and pulse-like rupture becomes the prominent failure mode. This fundamental change is caused by the finite amount of strain energy available for rupture under imposed-displacement boundary conditions. Such transition is analogous to the change in the rupture dynamics reported in three-dimensional simulations of earthquake ruptures with large aspect ratio $L \gg W$ (Day, 1982; Weng & Ampuero, 2019) or if the fault is surrounded by a damaged region with high elastic contrast (Idini & Ampuero, 2020). As depicted in Fig. 1, the relevant type of boundary conditions applied at a distance H from the fault corresponds to imposed-displacement. For subduction zones (Fig. 1a), the plate is loaded by and coupled to the downward motion of the viscous upper mantle. Due to the no-slip boundary conditions between the elastic plate and the viscous upper mantle, a constant displacement at the plate edge is a reasonable approximation over the duration of the dynamic ruptures. For the strike-slip system (Fig. 1b), slip along the fault leads to an associated stress drop in the compliant elastic fault core of thickness H. The continuity of displacements and stress at the boundary between the compliant fault core and the stiffer wall-rock implies that the associated displacement at this boundary will be much smaller than interfacial slip. Therefore, imposed-displacement boundary conditions is also relevant in such configurations. (see section C2 of Thøgersen et al. (2021) for more details).

Recently, Weng and Ampuero (2019) showed how the Linear Elastic Fracture Mechanics solution for a thin-strip geometry (Marder, 1998) can accurately describe earthquake dynamics at high aspect ratio L/W. Using the thin-strip solution, they proposed a *fault rupture potential* than can be used to predict the arrest and the size of earthquakes. As detailed in Section S.5, their thin-strip solution and associated fault rupture potential are complementary to the approach proposed in the present study, which brings estimates of the final slip profile and associated stress drop and generalizes the description beyond the Linear Elastic Fracture Mechanics assumption (finite fracture energy, small scale-yielding conditions, smooth rupture acceleration). Remarkably, the two descriptions share the same fracture energy criterion to predict rupture deceleration, i.e. $\bar{d}_c/\bar{d}_c^* = G_c/G_0 > 1$ and lead to similar arrest length prediction in the limit $\bar{d}_c \to \bar{d}_c^*$ (see Fig. S4).

5.2 Natural controls on rupture arrest

Previous studies have proposed that earthquake rupture may be arrested by the following situations:

- Low amount of available elastic strain energy, where the rupture enters a region that precludes a stress drop (Husseini et al., 1975). This mechanism is related to a stress heterogeneity barrier, where an uneven stress distribution, e.g. as induced by the history of past earthquakes, stops the earthquake (Aki, 1979).
- Barriers along the trajectory of the rupture, such as increase in fracture energy or geometrical heterogeneities may arrest a rupture. Such situations can arise when the rupture enters a region of intact rock at a fault tip (Husseini et al., 1975)) or along fault geometrical barriers such as bends, steps and jogs (Aki, 1979; Harris et al., 2002; Magistrale & Day, 1999).

Our minimal model is able to represent these arrest scenarios with only two control parameters in case of Amontons Coulomb friction ($\bar{\tau}_k$ and $\bar{\gamma}$), and with three parameters ($\bar{\tau}_k, \bar{d}_c$, and $\bar{\gamma}$) in case of slip-weakening friction. The most important parameters are the pre-stress, $\bar{\tau}_k$, and the fracture energy, $\bar{d}_c$. As discussed in the previous section, the one-dimensional slip pulse solution associated with imposed-displacement boundary conditions ($\Gamma = 1$) provides an accurate description of large planar earthquake rupture depicted in Fig. 1. In this context, we propose a pulse equation, summarized hereafter, that describes the propagation and arrest of frictional rupture:

$$\frac{\partial^2 \bar{u}_p}{\partial \bar{x}^2} = \bar{\gamma}\bar{u}_p - \eth\bar{\tau}_k. \tag{33}$$

We recall that $\bar{\tau}_k$ describes the pre-stress along the fault before the rupture, $\bar{u}_p$ corresponds to the total slip observed along the fault after the rupture, and $\eth$ is a parameters defined in Eq. (22) and whose value lies between 1 (for the largest admissible fracture energy) and 2 (for negligible fracture energy). We next discuss how to connect the natural arrest scenarios presented above, to the different scenarios of uneven distributions of pre-stress and fracture energy analysed for our minimal model.

5.2.1 Geometrical barriers – fault bends

Fault bends are observed to stop or slow ruptures (e.g. (Elliott et al., 2015; King & Nábělek, 1985)). One can parameterize this geometrical structure by a change in pre-

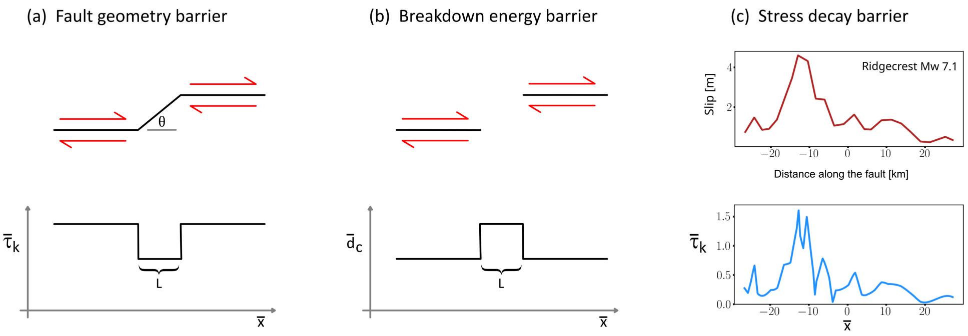

Figure 9. Cartoon of arrest scenarios and how they correspond to the different arrest scenarios discussed in Figure 3. a) A fault bend with an angle θ and length L corresponds to a decrease in $\bar{\tau}_k$. b) A fault step with offset of length L corresponds to a fracture energy barrier, and is represented by a lateral increase of $\bar{d}_c$ in our model. c) Top plot shows the profile of slip from the M_w7.1 2019 Ridgecrest earthquake published by Chen et al. (2020). The bottom plot shows the corresponding profile of dimensionless prestress computed using our pulse equation (33). See more details in section S.6.

stress (e.g. (Lozos et al., 2011)). For example, Fig. 9a illustrates a restraining bend. After projection of remotely applied principle stresses on inclined planes, it is readily shown that the shear stress, τ_0, on the bend segment is reduced relative to the straight fault segments, while the normal stress σ_n on the bend is increased relative to the straight fault segment, which we assume is favorably oriented for sliding. Both these trends act to reduce the ratio $\bar{\tau}_0/\sigma_n$ in Eq. (3) on the bend. Therefore, a restraining bend (Fig. 9a) is a similar scenario to the stress barrier displayed in Fig. 4B. Since scaling in Eq. (3) assumed a constant σ_n, we note that the calculation of $\bar{\tau}_k$ must be modified to account for spatially varying $\sigma_n(x)$ and to quantify the reduction of pre-stress over the bend segment.

As sketched in Fig. 9a, the amplitude of the pre-stress within the barrier depends on the angle of the restraining bend θ and its length depends on the bend segment length. One can therefore use our minimal model to predict quantitatively at which angles and which lengths of bend segments the rupture will stop. Our pulse arrest relationship of Eq. (19), and the corresponding Figure 5A, predict that the steeper the bend angle, the shorter the arrest length will be because $\bar{\tau}_{k,b}$ will decrease with increasing bend angle.

Thus, we can qualitatively predict that pulses will traverse relatively long shallowly inclined bends, but will be stopped by much shorter steep bends, in agreement with the figure 4b in Lozos et al. (2011).

For cracks, Eq. (30) predicts a different arrest scenario than for pulses. While pulse arrest is independent of where a fault bend is located relative to the hypocenter, under constant stress boundary conditions cracks should be able to traverse longer and steeper bends the further they are from the hypocenter, since they release more and more energy.

5.2.2 Geometrical barrier – step-overs and offsets

It is known that earthquakes often stop at fault step-overs or offsets, a situation depicted in Fig. 9b, upper panel. Barka and Kadinsky-Cade (1988) suggested that fault step-overs and offsets exceeding five kilometers and angles exceeding 30^o mostly stop earthquakes. Here, we follow Husseini et al. (1975) and suggest that the region of the step-over, which contains unbroken rock, can be described as a region with larger fracture energy, as in Fig. 9b. We showed in Fig. 5B that for pulses the arrest length $\bar{L}_{arr}$ increases as the material in the step-over between segments becomes weaker, i.e. $\bar{d}_c$ decreases. The value of $\bar{L}_{arr}$ is shown to range between $\sim 1{-}10$. If we bring this back to dimensional terms, the arrest length is in the range $H{-}10H$. In the scenario described in Fig. 1B, H corresponds to the thickness of the damage zone, which for mature strike-slip faults is in the range of few hundreds of meters to few kilometers (Ben-Zion & Sammis, 2003; Rockwell & Ben-Zion, 2007). Thus, the observations of Barka and Kadinsky-Cade (1988) are consistent with our predictions. Moreover, our model predicts that the thicker the damage zone the larger the offsets the earthquake can traverse.

5.2.3 Variable stress conditions

In the Earth's crust, the pre-stress along fault varies continuously due to tectonic loading, spatially and temporally varying slip, and earthquake-induced Coulomb stress transfer to and from neighboring faults. These processes increase or decrease pre-stress magnitude and heterogeneity with time. For example, Mildon et al. (2019) showed that the magnitude of pre-stress heterogeneity on faults in the Apennines exceeds 5 MPa, due to cumulative addition of Coulomb stress transfer of known earthquakes from the last 660 years, and an additional strong pre-stress heterogeneous component arising from irregular fault geometry, in particular from bends on faults, as discussed in the Section 5.2.1 above. Other works also find that pre-stress varies due to fault geometrical heterogeneities such as fault bends (e.g. Duan and Oglesby (2005)), fault roughness (e.g. Fang & Dunham, 2013; Cattania & Segall, 2021), or fault segmentation (e.g. Harris et al. (2002)). Examples of pre-stress variations unrelated to fault geometry include the 1966 Parkfield earthquake arrest, attributed to a seismic velocity anomaly in the lower crust (Aki, 1979), and pore pressure injections that may extend induced earthquake size (Galis et al., 2017). On top of the initial variability in pre-stress, each subsequent rupture event further evolves the pre-stress (Duan & Oglesby, 2005)).

Remarkably, the pulse equation (33) proposed in the present study allows for deducing the initial stress at the interface from the final slip profile. As example, Fig. 9c shows an application of equation (33) to slip data from the M_w7 Ridgecrest earthquake in 2019. As presented in the figure 2 of Chen et al. (2020), the rupture dynamics in the later stage of the rupture becomes similar to the one-dimensional planar pulse discussed in the present study. Therefore, we use the the profile of surface slip caused by the earthquake computed by Chen et al. (2020) using optical correlation of satellite images (shown in the top panel of Fig. 9c) and plug it into our pulse equation (33) to get an estimation of the stress profile before the rupture (shown in the bottom panel of Fig. 9c). The section S.6 provides additional information on the slip inversion process and the parameters used to produce Fig. 9c.

5.3 Planar pulse versus circular crack

The one-dimensional pulse rupture discussed in the present study has some important differences with the dynamics of circularly growing crack, each of them representing two end-member situations of the earthquake cycle: the circular crack model describes the early stage of a seismic rupture (radial growth, rupture size much smaller than the domain, unbounded available strain energy) whereas the planar pulse regime corresponds to the advanced stage of the rupture (planar front, rupture size larger than the domain dimensions H and W, limited available strain energy). Such a transition from crack to pulse once the crack saturates the seismogenic layer, is observed to occur in large strike-slip earthquakes, for example the 2019 $M_w7.1$ Ridgecrest earthquake (Chen et al., 2020), and the 2021 $M_w7.4$ Madoi earthquake (Chen et al., 2022). Apart from stable pulse-like solution discussed previously, planar rupture produces some interesting features of earthquake dynamics that remains debated in the circular-crack framework and could be explored in prospective works.

5.3.1 Stress drop

Using the pulse equation (33), the state of stress after the rupture can be predicted from the slip profile $\bar{u}_p$. As detailed in Eqs. (S.57)-(S.58), the stress drop in the one-dimensional model is given by $\eth\bar{\tau}_k$ or, in dimensional units,

$$\Delta\tau = \eth(\tau_0 - \mu_k\sigma_n), \tag{34}$$

Unlike circular cracks, planar pulse-like ruptures have then a stress drop independent of the rupture radius/size and proportional to the initial state of shear stress τ_0 acting on the fault before the event. Interestingly, this property of one-dimensional planar rupture implies that the final slip profile measured along fault zones after an earthquake provides information both on the initial shear stress before the rupture (as described in Figure 9c) but also after the rupture by subtracting the stress drop predicted in Eq. (34).

5.3.2 Back-propagating fronts at the arrest location

During the rupture arrests simulated in this paper, back-propagating fronts are sometimes observed after the sharp arrest of the main pulse front (e.g. by a stress or fracture energy barriers). As displayed in Figure S6, such fronts correspond to pulses of negative slip velocity that nucleate at the arrest location and propagate back to the nucleation zone. Back-propagating fronts are direct consequences of the stress drop described in Eq. (34) and the fact that one-dimensional planar rupture can reverse the sign of the shear stress along the interface. If the resulting negative shear stress is below the kinetic friction for negative slip (i.e. $\tau_0 - \Delta\tau < -\mu_k\sigma_n$), the interface is critically loaded and can host back-propagating fronts. Section S.7 and Figure S6 discuss how these secondary ruptures can be described by the same pulse theory presented in this paper and arise if the initial shear stress satisfies the following criterion:

$$\tau_0 > \frac{\eth + 1}{\eth - 1}\mu_k\sigma_n \geq 3\mu_k\sigma_n. \tag{35}$$

Recently, Idini and Ampuero (2020) reported travelling back-propagating fronts in numerical simulations of earthquake cycles within a low-velocity fault zone and discuss how recent progress in seismic monitoring allowed to detect secondary rupture fronts propagating with a reverse slip direction compared to the main rupture event. The presence of this low-velocity fault core (as shown in Fig. 1) and the pulse-like nature of these back-propagating fronts suggest some direct analogies with the response of our one-dimensional model.

5.3.3 Triangular slip profile

Slip profiles of faults and earthquakes often display a triangular shape (Manighetti et al., 2001, 2004, 2005; Scholz, 2019). These profiles have been observed to have a characteristic asymmetry, where the short edge of the triangle is usually closer to the hypocenter of the earthquake, the position of the maximum slip position is not constant, and the ratio between the two edges of the triangle varies among earthquakes (Manighetti et al., 2005). So far only a few models have been proposed to explain this observation. Manighetti et al. (2004) suggested that off-fault damage and plasticity account for the triangular slip distribution. Because, the presence of damage decreases the elastic moduli, Cappa et al. (2014) suggested that the moduli of the off-fault damaged zone varies along the fault. They demonstrated that this variation produces a triangular profile. In fact, this variation of moduli will produce a variation in available strain energy stored along the fault, and therefore this is equivalent to the slip pulse evolution when there is a depletion of strain energy scenario, that we describe in Figs. 3D and 6. Thus, $\bar{\tau}_k$ in our model encapsulates the backbone physics of the scenario of Manighetti et al. (2004) and Cappa et al. (2014), yet offers a larger set of scenarios for obtaining triangular slip: any slip pulse that propagates into regions of decreasing pre-stress or elastic strain energy will produce such a profile. In fact, our work suggests that triangular slip profiles may be a signature of pulse-like earthquakes that have been stopped by a depletion in available strain energy, which translates into depletion in $\bar{\tau}_k$.

6 Conclusion

To study frictional rupture arrest, we present a one-dimensional model that brings a characteristic length scale H to the standard Burridge-Knopoff model and bridges it to continuum fault models. The model captures the two types of boundary conditions relevant at the early and late stage of earthquake rupture and reveals their fundamental impact on the style of the rupture (crack versus pulse), its energy balance, and the arrest conditions. Under imposed-displacement boundary conditions, the proposed one-dimensional model provides a good approximation for the dynamics of large earthquake ruptures that saturate the width of the seismogenic zone and propagate as planar front (as sketched in Figure 1). In this context, the main conclusions are:

- The formulation of the model is minimal and generic and allows to wrap various earthquake arrest scenarios into the variations of two dimensionless variables $\bar{\tau}_k$ (initial pre-stress on the fault) and $\bar{d}_c$ (fracture energy).
- Using these two parameters, we propose simple scaling relationships to characterize the arrest length of earthquakes.
- The stress drop is directly proportional to the initial pre-stress.
- The regions of the fault that will arrest the next large earthquake can be predicted independently of where the rupture will nucleate.
- The transition from circular crack growth to the propagation of planar pulse brings new insight on unsettled features of natural earthquakes such as the observed asymmetric, triangular, slip profile along fault zones, the conditions for back-propagating ruptures, and the prevalence of the pulse-like rupture style for large earthquakes.
- The present paper focuses on earthquake dynamics, but the generality of the proposed one-dimensionless formulation may find applications in other geological settings where the size of the rupture exceeds the width of the surrounding bulk, such as landslides, glacier surge, and snow avalanches (Thøgersen, Gilbert, et al., 2019; Trottet et al., 2022).

Acknowledgments

This project has received funding from the Research Council of Norway (project "History Dependent Friction", grant No. 287084) and the European Research Council (ERC) under the European Union's Horizon 2020 research and innovation program (grant agreement No. 101019628 BREAK). All the data necessary to reproduce the results are given in the main text and the code for the numerical model is available at: github.com/kjetilthogersen/1D-rupture

List of main symbols

$\bar{x}$	Position along the fault
$\bar{t}$	Time
$\bar{u}$	Slip
$\bar{\tau}$	Shear stress
$\bar{\tau}_f$	Frictional stress
$\bar{\Gamma}$	Boundary conditions: imposed-stress ($\Gamma = 0$) or imposed-displacement ($\Gamma = 1$)
$\bar{\gamma}$	Elastic modulus parameter
$\bar{\tau}_k$	Pre-stress
$\bar{d}_c$	Critical weakening distance
$\bar{G}_c = \bar{d}_c/2$	Fracture energy
$\bar{K}$	One-dimensional stress intensity factor
$\bar{W}_b$	Breakdown work
$\bar{E}_{\text{el}}$	Elastic energy
$\bar{E}_{\text{kin}}$	Kinetic energy
$\bar{W}_{\text{ext}}$	External work
$\bar{v}_c$	Rupture propagation speed
$\bar{u}_p$	Final slip (i.e. after rupture arrest)
$\bar{\beta}$	Numerical damping
$\bar{\mathcal{L}}$	Length of the domain
$\bar{L}$	Rupture length
$\bar{L}_{\text{arr}}$	Arrest length
x	Position
t	Time
u_i	Displacement
$\hat{u}_0$	Imposed displacement at the top boundary
$\langle u_i \rangle$	Average displacement over the block height
σ_{ij}	Cauchy stress tensor
σ_n	Normal stress at the interface
τ_f	Frictional (shear) stress at the interface
H	Height of the solid block
λ	Lamé first coefficient
$\mathcal{G}$	Shear modulus
ρ	Solid density
μ_s	Static friction coefficient
μ_k	Dynamic friction coefficient
d_c	Critical slip weakening distance

Table 1. List of variables used in the manuscript and the Supplementary Information. The dashed line separates the dimensionless variables (above) and the variables with dimensions (below). See also Table S1 for further information on how to relate these variables to dimensional quantities.

References

Abercrombie, R. E., & Rice, J. R. (2005). Can observations of earthquake scaling constrain slip weakening? *Geophysical Journal International*, *162*(2), 406–424.

Agliardi, F., Scuderi, M. M., Fusi, N., & Collettini, C. (2020). Slow-to-fast transition of giant creeping rockslides modulated by undrained loading in basal shear zones. *Nature communications*, *11*(1), 1–11.

Aki, K. (1979). Characterization of barriers on an earthquake fault. *Journal of Geophysical Research: Solid Earth*, *84*(B11), 6140–6148.

Amundsen, D. S., Scheibert, J., Thøgersen, K., Trømborg, J., & Malthe-Sørenssen, A. (2012). 1D Model of Precursors to Frictional Stick-Slip Motion Allowing for Robust Comparison with Experiments. *Tribology Letters*, *45*(2), 357–369. doi: 10.1007/s11249-011-9894-3

Barka, A., & Kadinsky-Cade, K. (1988). Strike-slip fault geometry in turkey and its influence on earthquake activity. *Tectonics*, *7*(3), 663–684.

Barras, F., Aldam, M., Roch, T., Brener, E. A., Bouchbinder, E., & Molinari, J.-F. (2020). The emergence of crack-like behavior of frictional rupture: Edge singularity and energy balance. *Earth and Planetary Science Letters*, *531*, 115978. doi: 10.1016/j.epsl.2019.115978

Bayart, E., Svetlizky, I., & Fineberg, J. (2016). Fracture mechanics determine the lengths of interface ruptures that mediate frictional motion. *Nature Physics*, *12*(2), 166–170. doi: 10.1038/nphys3539

Ben-Zion, Y., & Sammis, C. G. (2003). Characterization of fault zones. *Pure and applied geophysics*, *160*(3), 677–715.

Brantut, N., Garagash, D. I., & Noda, H. (2019). Stability of Pulse-Like Earthquake Ruptures. *Journal of Geophysical Research: Solid Earth*, *124*(8), 8998–9020. doi: 10.1029/2019JB017926

Braun, O. M., Barel, I., & Urbakh, M. (2009). Dynamics of Transition from Static to Kinetic Friction. *Physical Review Letters*, *103*(19), 194301. doi: 10.1103/PhysRevLett.103.194301

Brener, E. A., Aldam, M., Barras, F., Molinari, J.-F., & Bouchbinder, E. (2018). Unstable Slip Pulses and Earthquake Nucleation as a Nonequilibrium First-Order Phase Transition. *Physical Review Letters*, *121*(23), 234302. doi: 10.1103/PhysRevLett.121.234302

Brener, E. A., & Bouchbinder, E. (2021). Unconventional singularities and energy balance in frictional rupture. *Nature Communications*, *12*(1), 2585. doi: 10.1038/s41467-021-22806-9

Brown, S. R., Scholz, C. H., & Rundle, J. B. (1991). A simplified spring-block model of earthquakes. *Geophysical Research Letters*, *18*(2), 215–218. doi: 10.1029/91GL00210

Burridge, R., & Halliday, G. (1971). Dynamic shear cracks with friction as models for shallow focus earthquakes. *Geophysical Journal International*, *25*(1-3), 261–283.

Burridge, R., & Knopoff, L. (1967). Model and theoretical seismicity. *Bulletin of the Seismological Society of America*, *57*(3), 341-371. Retrieved from `https://doi.org/10.1785/BSSA0570030341` doi: 10.1785/BSSA0570030341

Cappa, F., Perrin, C., Manighetti, I., & Delor, E. (2014). Off-fault long-term damage: A condition to account for generic, triangular earthquake slip profiles. *Geochemistry, Geophysics, Geosystems*, *15*(4), 1476-1493.

Carlson, J. M., Langer, J. S., & Shaw, B. E. (1994). Dynamics of earthquake faults. *Reviews of Modern Physics*, *66*(2), 657–670. doi: 10.1103/RevModPhys.66.657

Cattania, C., & Segall, P. (2021). Precursory Slow Slip and Foreshocks on Rough Faults. *Journal of Geophysical Research: Solid Earth*, *126*(4), e2020JB020430. doi: 10.1029/2020JB020430

Chen, K., Avouac, J.-P., Aati, S., Milliner, C., Zheng, F., & Shi, C. (2020, January). Cascading and pulse-like ruptures during the 2019 Ridgecrest earthquakes in the Eastern California Shear Zone. *Nature Communications*, *11*(1), 22. doi: 10.1038/s41467-019-13750-w

Chen, K., Avouac, J.-P., Geng, J., Liang, C., Zhang, Z., Li, Z., & Zhang, S. (2022). The 2021 mw 7.4 madoi earthquake: An archetype bilateral slip-pulse rupture arrested at a splay fault. *Geophysical Research Letters*, *49*(2), e2021GL095243.

Cromer, A. (1981). Stable solutions using the Euler approximation. *American Journal of Physics*, *49*(5), 455–459. doi: 10.1119/1.12478

Das, S., & Aki, K. (1977). Fault plane with barriers: a versatile earthquake model. *Journal of Geophysical Research*, *82*(36), 5658–5670.

Day, S. M. (1982). Three-dimensional finite difference simulation of fault dynamics: Rectangular faults with fixed rupture velocity. *Bulletin of the Seismological Society of America*, *72*(3), 705–727. doi: 10.1785/BSSA0720030705

Duan, B., & Oglesby, D. D. (2005). Multicycle dynamics of nonplanar strike-slip faults. *Journal of Geophysical Research: Solid Earth*, *110*(B3).

Elbanna, A. E., & Heaton, T. H. (2012). A new paradigm for simulating pulse-like ruptures: the pulse energy equation. *Geophysical Journal International*, *189*(3), 1797–1806.

Elliott, A. J., Oskin, M. E., Liu-Zeng, J., & Shao, Y. (2015). Rupture termination at restraining bends: The last great earthquake on the altyn tagh fault. *Geophysical Research Letters*, *42*(7), 2164–2170.

Fang, Z., & Dunham, E. M. (2013). Additional shear resistance from fault roughness and stress levels on geometrically complex faults. *Journal of Geophysical Research: Solid Earth*, *118*(7), 3642–3654. doi: 10.1002/jgrb.50262

Freund, L. B. (1998). *Dynamic fracture mechanics*. Cambridge university press.

Gabriel, A.-A., Ampuero, J.-P., Dalguer, L. A., & Mai, P. M. (2012). The transition of dynamic rupture styles in elastic media under velocity-weakening friction. *Journal of Geophysical Research: Solid Earth*, *117*(B9).

Galis, M., Ampuero, J. P., Mai, P. M., & Cappa, F. (2017). Induced seismicity provides insight into why earthquake ruptures stop. *Science advances*, *3*(12), eaap7528.

Gvirtzman, S., & Fineberg, J. (2021). Nucleation fronts ignite the interface rupture that initiates frictional motion. *Nature Physics*, *17*(9), 1037–1042.

Harris, R. A., & Day, S. M. (1999). Dynamic 3d simulations of earthquakes on en echelon faults. *Geophysical Research Letters*, *26*(14), 2089–2092.

Harris, R. A., Dolan, J. F., Hartleb, R., & Day, S. M. (2002). The 1999 izmit, turkey, earthquake: A 3d dynamic stress transfer model of intraearthquake triggering. *Bulletin of the Seismological Society of America*, *92*(1), 245–255.

Heaton, T. H. (1990). Evidence for and implications of self-healing pulses of slip in earthquake rupture. *Physics of the Earth and Planetary Interiors*, *64*(1), 1–20. doi: 10.1016/0031-9201(90)90002-F

Husseini, M. I., Jovanovich, D. B., Randall, M., & Freund, L. (1975). The fracture energy of earthquakes. *Geophysical Journal International*, *43*(2), 367–385.

Ida, Y. (1972, July). Cohesive force across the tip of a longitudinal-shear crack and Griffith's specific surface energy. *Journal of Geophysical Research*, *77*(20), 3796–3805. doi: 10.1029/JB077i020p03796

Idini, B., & Ampuero, J.-P. (2020). Fault-Zone Damage Promotes Pulse-Like Rupture and Back-Propagating Fronts via Quasi-Static Effects. *Geophysical Research Letters*, *47*(23). doi: 10.1029/2020GL090736

Kammer, D. S., Radiguet, M., Ampuero, J.-P., & Molinari, J.-F. (2015). Linear Elastic Fracture Mechanics Predicts the Propagation Distance of Frictional Slip. *Tribology Letters*, *57*(3), 23. doi: 10.1007/s11249-014-0451-8

Ke, C.-Y., McLaskey, G. C., & Kammer, D. S. (2018). Rupture Termination in Laboratory-Generated Earthquakes. *Geophysical Research Letters*, *45*(23). doi: 10.1029/2018GL080492

Ke, C.-Y., McLaskey, G. C., & Kammer, D. S. (2022). Earthquake breakdown energy scaling despite constant fracture energy. *Nature Communications*, *13*(1), 1005. doi: 10.1038/s41467-022-28647-4

King, G., & Nábělek, J. (1985). Role of fault bends in the initiation and termination of earthquake rupture. *Science*, *228*(4702), 984–987.

Knopoff, L., & Ni, X. X. (2001). Numerical Instability at the Edge of a Dynamic Fracture. *Geophysical Journal International*, *147*(3), 1–6. doi: 10.1046/j.1365-246x.2001.01567.x

Kostrov, B. (1966). Unsteady propagation of longitudinal shear cracks. *Journal of Applied Mathematics and Mechanics*, *30*(6), 1241–1248.

Kostrov, B., & Das, S. (1988). *Principles of earthquake source mechanics.* Cambridge University Press.

Lambert, V., & Lapusta, N. (2020). Rupture-dependent breakdown energy in fault models with thermo-hydro-mechanical processes. *Solid Earth*, *11*(6), 2283–2302. doi: 10.5194/se-11-2283-2020

Lambert, V., Lapusta, N., & Perry, S. (2021). Propagation of large earthquakes as self-healing pulses or mild cracks. *Nature*, *591*(7849), 252–258. doi: 10.1038/s41586-021-03248-1

Lozos, J. C., Oglesby, D. D., Duan, B., & Wesnousky, S. G. (2011). The effects of double fault bends on rupture propagation: A geometrical parameter study. *Bulletin of the Seismological Society of America*, *101*(1), 385–398.

Madariaga, R. (1976). Dynamics of an expanding circular fault. *Bulletin of the Seismological Society of America*, *66*(3), 639–666.

Magistrale, H., & Day, S. (1999). 3d simulations of multi-segment thrust fault rupture. *Geophysical Research Letters*, *26*(14), 2093–2096.

Manighetti, I., Campillo, M., Sammis, C., Mai, P. M., & King, G. (2005). Evidence for self-similar, triangular slip distributions on earthquakes: Implications for earthquake and fault mechanics. *Journal of Geophysical Research: Solid Earth*, *110*(B5).

Manighetti, I., King, G., Gaudemer, Y., Scholz, C., & Doubre, C. (2001). Slip accumulation and lateral propagation of active normal faults in afar. *Journal of Geophysical Research: Solid Earth*, *106*(B7), 13667–13696.

Manighetti, I., King, G., & Sammis, C. G. (2004). The role of off-fault damage in the evolution of normal faults. *Earth and Planetary Science Letters*, *217*(3-4), 399–408.

Manighetti, I., Zigone, D., Campillo, M., & Cotton, F. (2009). Self-similarity of the largest-scale segmentation of the faults: Implications for earthquake behavior. *Earth and Planetary Science Letters*, *288*(3-4), 370–381.

Marder, M. (1998). Adiabatic equation for cracks. *Philosophical Magazine B*, *78*(2), 203–214. doi: 10.1080/13642819808202942

Marone, C., & Scholz, C. (1988). The depth of seismic faulting and the upper transition from stable to unstable slip regimes. *Geophysical Research Letters*, *15*(6), 621–624.

Mildon, Z., Roberts, G. P., Walker, J. F., & Toda, S. (2019). Coulomb pre-stress and fault bends are ignored yet vital factors for earthquake triggering and hazard. *Nature communications*, *10*(1), 1–9.

Olami, Z., Feder, H. J. S., & Christensen, K. (1992). Self-organized criticality in a continuous, nonconservative cellular automaton modeling earthquakes. *Physical Review Letters*, *68*(8), 1244–1247. doi: 10.1103/PhysRevLett.68.1244

Paglialunga, F., Passelègue, F., Brantut, N., Barras, F., Lebihain, M., & Violay, M. (2021). On the scale dependence in the dynamics of frictional rupture: Constant fracture energy versus size-dependent breakdown work. *arXiv:2104.15103 [physics]*.

Palmer, A. C., & Rice, J. R. (1973). The growth of slip surfaces in the progressive failure of over-consolidated clay. *Proceedings of the Royal Society of London. A. Mathematical and Physical Sciences*, *332*(1591), 527–548. doi: 10.1098/rspa.1973.0040

Perrin, C., Manighetti, I., Ampuero, J.-P., Cappa, F., & Gaudemer, Y. (2016). Location of largest earthquake slip and fast rupture controlled by along-strike change in fault structural maturity due to fault growth. *Journal of Geophysical Research: Solid Earth*, *121*(5), 3666–3685.

Roch, T., Brener, E. A., Molinari, J.-F., & Bouchbinder, E. (2022). Velocity-driven frictional sliding: Coarsening and steady-state pulses. *Journal of the Mechanics and Physics of Solids*, *158*, 104607. doi: 10.1016/j.jmps.2021.104607

Rockwell, T. K., & Ben-Zion, Y. (2007). High localization of primary slip zones in large earthquakes from paleoseismic trenches: Observations and implications for earthquake physics. *Journal of Geophysical Research: Solid Earth*, *112*(B10).

Scholz, C. H. (1998). Earthquakes and friction laws. *Nature*, *391*(6662), 37–42.

Scholz, C. H. (2019). *The Mechanics of Earthquakes and Faulting* (Third ed.). Cambridge University Press. doi: 10.1017/9781316681473

Sibson, R. H. (1985). Stopping of earthquake ruptures at dilational fault jogs. *Nature*, *316*(6025), 248–251.

Sibson, R. H., & Das, S. (1986). Rupture interaction with fault jogs. *Earthquake Source Mechanics*, *37*, 157–167.

Thøgersen, K., Aharonov, E., Barras, F., & Renard, F. (2021). Minimal model for the onset of slip pulses in frictional rupture. *Physical Review E*, *103*(5), 052802. doi: 10.1103/PhysRevE.103.052802

Thøgersen, K., Gilbert, A., Schuler, T. V., & Malthe-Sørenssen, A. (2019). Rate-and-state friction explains glacier surge propagation. *Nature Communications*, *10*(1), 2823. doi: 10.1038/s41467-019-10506-4

Thøgersen, K., Sveinsson, H., Scheibert, J., Renard, F., & Malthe-Sørenssen, A. (2019). The moment duration scaling relation for slow rupture arises from transient rupture speeds. *Geophysical Research Letters*, *46*(22), 12805–12814.

Tinti, E., Spudich, P., & Cocco, M. (2005). Earthquake fracture energy inferred from kinematic rupture models on extended faults. *Journal of Geophysical Research*, *110*(B12), B12303. doi: 10.1029/2005JB003644

Trømborg, J., Scheibert, J., Amundsen, D. S., Thøgersen, K., & Malthe-Sørenssen, A. (2011). Transition from Static to Kinetic Friction: Insights from a 2D Model. *Physical Review Letters*, *107*(7), 074301. doi: 10.1103/PhysRevLett.107.074301

Trømborg, J., Sveinsson, H., Scheibert, J., Thøgersen, K., Amundsen, D. S., & Malthe-Sørenssen, A. (2014). Slow slip and the transition from fast to slow fronts in the rupture of frictional interfaces. *Proceedings of the National Academy of Sciences*, *111*(24), 8764–8769. doi: 10.1073/pnas.1321752111

Trottet, B., Simenhois, R., Bobillier, G., Bergfeld, B., van Herwijnen, A., Jiang, C., & Gaume, J. (2022). Transition from sub-Rayleigh anticrack to supershear crack propagation in snow avalanches. *Nature Physics*, *18*(9), 1094–1098. Retrieved from `https://www.nature.com/articles/s41567-022-01662-4` doi: 10.1038/s41567-022-01662-4

Viesca, R. C., & Rice, J. R. (2012). Nucleation of slip-weakening rupture instability in landslides by localized increase of pore pressure. *Journal of Geophysical Research: Solid Earth*, *117*(B3). doi: 10.1029/2011JB008866

Weng, H., & Ampuero, J.-P. (2019). The Dynamics of Elongated Earthquake Ruptures. *Journal of Geophysical Research: Solid Earth*, *124*(8), 8584–8610. doi: 10.1029/2019JB017684

Wesnousky, S. G. (1988). Seismological and structural evolution of strike-slip faults. *Nature*, *335*(6188), 340–343.

Zheng, G., & Rice, J. R. (1998). Conditions under which velocity-weakening friction allows a self-healing versus a cracklike mode of rupture. *Bulletin of the Seismological Society of America*, *88*(6), 1466–1483. doi: 10.1785/BSSA0880061466

Supporting Information for "How do earthquakes stop? Insights from a minimal model of frictional rupture"

Fabian Barras[1], Kjetil Thøgersen[1], Einat Aharonov[1,2], François Renard[1,3]

[1]The Njord Centre, Departments of Geosciences and Physics, box 1048, University of Oslo, Blindern, 0316 Oslo, Norway

[2]Institute of Earth Sciences, The Hebrew University, Jerusalem, 91904, Israel

[3]ISTerre, Univ. Grenoble Alpes, Grenoble INP, Univ. Savoie Mont Blanc, CNRS, IRD, Univ. Gustave Eiffel, 38000, Grenoble, France

The Supporting Information contains a list of main symbols, one table, six figures, and seven supplementary text sections.

List of main symbols

$\bar{x}$	Position along the fault
$\bar{t}$	Time
$\bar{u}$	Slip
$\bar{\tau}$	Shear stress
$\bar{\tau}_f$	Frictional stress
$\bar{\Gamma}$	Boundary conditions: imposed-stress ($\Gamma = 0$) or imposed-displacement ($\Gamma = 1$)
$\bar{\gamma}$	Elastic modulus parameter
$\bar{\tau}_k$	Pre-stress
$\bar{d}_c$	Critical weakening distance
$\bar{G}_c = \bar{d}_c/2$	Fracture energy
$\bar{K}$	One-dimensional stress intensity factor
$\bar{W}_b$	Breakdown work
$\bar{E}_{\mathrm{el}}$	Elastic energy
$\bar{E}_{\mathrm{kin}}$	Kinetic energy
$\bar{W}_{\mathrm{ext}}$	External work
$\bar{v}_c$	Rupture propagation speed
$\bar{u}_p$	Final slip (i.e. after rupture arrest)
$\bar{\beta}$	Numerical damping
$\bar{\mathcal{L}}$	Length of the domain
$\bar{L}$	Rupture length
$\bar{L}_{\mathrm{arr}}$	Arrest length
x	Position
t	Time
u_i	Displacement
$\hat{u}_0$	Imposed displacement at the top boundary
$\langle u_i \rangle$	Average displacement over the block height
σ_{ij}	Cauchy stress tensor
σ_n	Normal stress at the interface
τ_f	Frictional (shear) stress at the interface
H	Height of the solid block
λ	Lamé first coefficient
$\mathcal{G}$	Shear modulus
ρ	Solid density
μ_s	Static friction coefficient
μ_k	Dynamic friction coefficient
d_c	Critical slip weakening distance

S.1. One-dimensional elastodynamic model

Let us consider the linear elastic block and associated system of coordinates presented in Figure 2. For each coordinate ($i = x, y, z$), the balance of linear momentum writes:

$$\rho \frac{\partial^2 u_i}{\partial t^2} = \frac{\partial \sigma_{xi}}{\partial x} + \frac{\partial \sigma_{yi}}{\partial y} + \frac{\partial \sigma_{zi}}{\partial z}, \tag{S.1}$$

where σ_{ij} are the components of the Cauchy stress tensor and u_i is the displacement field. Next, we assume that the normal stress is homogeneous and constant ($\sigma_{yy}(x, y, z, t) \equiv \sigma_n$) and that the elastic fields are invariant in the out-of-plane direction ($\partial u_i / \partial_z = 0$), such that the momentum balance equation becomes

$$\rho \frac{\partial^2 u_i}{\partial t^2} = \Lambda \frac{\partial^2 u_i}{\partial x^2} + \frac{\partial \sigma_{yi}}{\partial y}. \tag{S.2}$$

The equation above applies equivalently to mode II displacement, for which i corresponds to x and $\Lambda = \lambda + 2\mathcal{G}$, and to mode III displacement, for which i corresponds to z and $\Lambda = \mathcal{G}$. The height of the system H is assumed to be small compared to the other dimensions of the problem, such that variations of u_i over y are small and the momentum balance can be solved in average across the height (Bouchbinder et al., 2011; Bar-Sinai et al., 2013). At time $t = 0$, the system is initially at rest, such that one can define the height-averaged displacement field as

$$\langle u_i \rangle_y(x, t) = \frac{1}{H} \int_0^H \Big(u_i(x, y, t) - u_i(x, y, 0) \Big) \mathrm{dy}, \tag{S.3}$$

with $u_i(x, y, 0)$ corresponding to the initial static displacement field. Using the definition of $\langle u_i \rangle_y$, both sides of Eq. (S.2) are integrated between zero and H to obtain the following one-dimensional formulation:

$$H\rho \frac{\partial^2 \langle u_i \rangle_y}{\partial t^2} = H\Lambda \frac{\partial^2 \langle u_i \rangle_y}{\partial x^2} + \sigma_{yi}(x, H, t) - \sigma_{yi}(x, 0, t). \tag{S.4}$$

Next, the boundary conditions on the top and bottom surfaces need to be applied. The shear stress on the bottom surface corresponds to the frictional stress:

$$\sigma_{yi}(x,0,t) \equiv \tau_f(x,t). \tag{S.5}$$

On the top surface, two kinds of boundary conditions can be considered:

$$\text{stress} - \text{controlled} : \sigma_{yi}(x,H,t) \equiv \tau_0(x) \tag{S.6}$$

$$\text{displacement} - \text{controlled} : u_i(x,H,t). \equiv \hat{u}_0(x) \tag{S.7}$$

For imposed stress, the value of the shear stress at the top boundary is fixed, whereas for imposed displacement $\sigma_{yi}(x,H,t)$ evolves with interfacial slip. To estimate this evolution, the displacement field through the height of the block can be expressed as the following Taylor expansion

$$u_i(x,y,t) = u_i(x,H,t) + (y-H)\frac{\partial u_i(x,y,t)}{\partial y}|_{y=H} + \mathcal{O}\Big((y-H)^2\Big). \tag{S.8}$$

In the right-hand side of the equation above, the first term corresponds to the imposed-displacement $\hat{u}_0$, the derivative in the second term corresponds to $\sigma_{yi}(x,H,t)/\mathcal{G}$ and the third term accounts for higher-order contributions that can be neglected as variations of u_i through H are small. Invoking that the initial static displacement field corresponds to $u_i(x,y,0) = \hat{u}_0(x)y/H$, the height-averaged displacement can be integrated following Eq. (S.3) as:

$$\langle u_i \rangle_y(x,t) = \frac{1}{2}\hat{u}_0(x) - \frac{H}{2\mathcal{G}}\sigma_{yi}(x,H,t). \tag{S.9}$$

From the equation above, $\sigma_{yi}(x,H,t)$ can then be expressed as an initial shear stress τ_0 related to the imposed displacement minus the elastic relaxation resulting from slip:

$$\sigma_{yi}(x,H,t) = \frac{\mathcal{G}}{H}\Big(\hat{u}_0(x) - 2\langle u_i \rangle_y(x,t)\Big) \equiv \tau_0(x) - \frac{2\mathcal{G}}{H}\langle u_i \rangle_y(x,t). \tag{S.10}$$

Using Eqs. (S.5), (S.6) and (S.10), the momentum equation (S.4) can be re-written as:

$$\frac{\partial^2 \langle u_i \rangle_y}{\partial t^2} = \frac{\Lambda}{\rho} \frac{\partial^2 \langle u_i \rangle_y}{\partial x^2} - \Gamma \frac{2\mathcal{G}}{\rho H^2} \langle u_i \rangle_y + \frac{1}{\rho H} \Big(\tau_0(x) - \tau_f(x,t) \Big), \tag{S.11}$$

where Γ is a binary parameter being equal to zero for stress boundary condition, and equal to one for displacement boundary condition on the top surface.

Following the normalization procedure summarized in Table S1, the one-dimensional momentum equation above can be re-written in the dimensionless form:

$$\frac{\partial^2 \bar{u}}{\partial \bar{t}^2} = \frac{\partial^2 \bar{u}}{\partial \bar{x}^2} - \Gamma \bar{\gamma} \bar{u} + \bar{\tau}, \tag{S.12}$$

which is Eq. (1) in the main text. In Table S1, the dimensionless shear stress is defined with respect to the static μ_s and kinematic μ_k coefficient of friction. For the example of linear slip-weakening friction with only positive slip velocities, the shear stress can be expressed as function of the deviation from residual friction $\bar{\tau}_f$:

$$\bar{\tau}(\bar{x}, \bar{t}) = \bar{\tau}_k(\bar{x}) - \bar{\tau}_f(\bar{x}, \bar{t}) \begin{cases} > \bar{\tau}_k - 1 & ,\text{if } \ \dot{\bar{u}} = 0 \\ = \bar{\tau}_k - (1 - \bar{u}/\bar{d}_c) & ,\text{if } \ 0 \le \bar{u} \le \bar{d}_c \ , \\ = \bar{\tau}_k & ,\text{if } \ \bar{u} > \bar{d}_c \end{cases} \tag{S.13}$$

with $\bar{d}_c$ being the critical slip distance and $\bar{\tau}_k$ the dimensionless residual friction defined in Eq. (3). Equation (S.13) also describes Amontons-Coulomb friction in the limit $\bar{d}_c = 0$.

S.2. Parameters and convergence of the numerical scheme

As described in Section 3 of the main text, the one-dimensional model is solved in space using a central finite-difference scheme with uniform grid size $\Delta\bar{x}$ and integrated in time following Euler-Cromer scheme (Cromer, 1981), with uniform time step $\Delta\bar{t}$. At time step j and element i, the integration of a slipping portion of the interface writes

$$\begin{cases} \ddot{\bar{u}}_i^j = \dfrac{\bar{u}_{i+1}^j - 2\bar{u}_i^j + \bar{u}_{i-1}^j}{(\Delta\bar{x})^2} - \Gamma\bar{\gamma}\bar{u}_i^j + \bar{\tau}_i + \bar{\beta}\dfrac{\dot{\bar{u}}_{i+1}^j - 2\dot{\bar{u}}_i^j + \dot{\bar{u}}_{i-1}^j}{(\Delta\bar{x})^2}, \\ \dot{\bar{u}}_i^{j+1} = \dot{\bar{u}}_i^j + \ddot{\bar{u}}_i^j\Delta\bar{t}, \\ \bar{u}_i^{j+1} = \bar{u}_i^j + \dot{\bar{u}}_i^{j+1}\Delta\bar{t}. \end{cases} \tag{S.14}$$

The one-dimensional model in its discretized model (S.14) is similar to the dynamics of Burridge-Knopoff models whose governing equation has the generic form:

$$m\ddot{u} - k(u_{i+1} - 2u_i + u_{i-1}) + lu_i - \eta(\dot{u}_{i+1} - 2\dot{u}_i + \dot{u}_{i-1}^k) = f_i, \tag{S.15}$$

with m being the mass of the block, k, l respectively the longitudinal and leaf spring constants and f_i the driving force. As described by Knopoff and Ni (2001), at the tip of a propagating rupture, the moving boundary between sticking and slipping portion of the fault creates numerical oscillations that can be removed by introducing a viscous damping term η. A spectral analysis of Eq. (S.15) shows that setting $\eta = \sqrt{km}$ implies that the spurious oscillations with grid-size wavelength are critically damped (Amundsen et al., 2012). In practice, Burridge-Knopoff models typically use a value of $\eta = \sqrt{0.1km}$ which provides the best compromise between reducing the numerical oscillations and not damping the physical rupture dynamics (Knopoff & Ni, 2001; Amundsen et al., 2012).

This value is adopted in our one-dimensional simulations with Amontons-Coulomb friction law. Using the analogy between Eqs. (S.14) and (S.15), this corresponds to $m = 1$, $k = (\Delta\bar{x})^{-2}$ and $\beta = \eta(\Delta\bar{x})^2 = \sqrt{0.1km}(\Delta\bar{x})^2 = \sqrt{0.1}\Delta\bar{x}$. This relative viscous damping term reduces the convergence rate from quadratic to linear but guarantees the stability of the numerical scheme for discontinuous problems as shown in Figure S1. $\Delta\bar{x} \leq 4\cdot 10^{-3}$ together with the Courant-Friedrichs–Lewy condition (Courant et al., 1928), $\Delta\bar{t} \leq 0.1\Delta\bar{x}$, have been adopted in the simulations reported in the present study to guarantee the numerical convergence.

S.3. Pulse equations

The pulse equation can be expressed by integrating the total energy between the nucleation position $\bar{x} = 0$ and the position of the leading head of the pulse $\bar{L}(\bar{t})$ at time $\bar{t}$ using Eqs. (12) to (14). Next, we assume that the width of the pulse is much smaller than the total ruptured length. This assumption allows us 1) to neglect the contribution of the kinetic energy which is only non-zero within the pulse and 2) to substitute $\bar{u}(\bar{x}, \bar{t})$ by the final slip $\bar{u}_p(\bar{x})$ observed in the wake of the pulse. The total energy at time $\bar{t}$ writes then:

$$\bar{E}(\bar{t}) = \int_0^{\bar{L}(\bar{t})} \left\{ \bar{\tau}_k \bar{u}_p - \bar{W}_b - \frac{1}{2}\left(\frac{\partial \bar{u}_p}{\partial \bar{x}}\right)^2 - \frac{1}{2}\bar{\gamma}\bar{u}_p^2 \right\} \mathrm{d}\bar{x}. \tag{S.16}$$

We next use integration by parts and the fact that $\bar{u}_p$ is zero at the two bounds of the integral above to rewrite the equation as:

$$\bar{E}(\bar{t}) = \int_0^{\bar{L}(\bar{t})} \left\{ \bar{\tau}_k \bar{u}_p - \bar{W}_b + \frac{1}{2}\bar{u}_p \frac{\partial^2 \bar{u}_p}{\partial \bar{x}^2} - \frac{1}{2}\bar{\gamma}\bar{u}_p^2 \right\} \mathrm{d}\bar{x} \tag{S.17}$$

Finally, the total energy should be conserved throughout pulse propagation, which implies that:

$$\frac{\mathrm{d}\bar{E}}{\mathrm{d}\bar{L}} = 0 = \bar{\tau}_k \bar{u}_p - \bar{W}_b + \frac{1}{2}\bar{u}_p \frac{\partial^2 \bar{u}_p}{\partial \bar{x}^2} - \frac{1}{2}\bar{\gamma}\bar{u}_p^2. \tag{S.18}$$

This pulse equation can be used to predict the final slip observed in the wake of pulse-like rupture as function of the profile of shear stress lumped in $\bar{\tau}_k(\bar{x})$ and the interface breakdown energy described by $\bar{W}_b$.

S.3.1. Amontons-Coulomb friction

With Amontons-Coulomb friction, the breakdown work is negligible ($\bar{W}_b = 0$). Excluding the trivial solution $\bar{u}_p = 0$, the final slip is given by the following second-order linear pulse equation:

$$\frac{\partial^2 \bar{u}_p}{\partial \bar{x}^2} = \bar{\gamma}\bar{u}_p - 2\bar{\tau}_k. \tag{S.19}$$

This pulse equation can be used for example to predict how $\bar{u}_p$ decays within a stress barrier by defining the initial value problem $u_p(\bar{x}' = 0) = 2\tau_{k,0}/\bar{\gamma}$ with $\bar{x}' = \bar{x} - \bar{x}_b$, which has a general solution given by two constants C_1 and C_2:

$$\bar{u}_p(\bar{x}') = \frac{2\bar{\tau}_{k,b}}{\bar{\gamma}} + C_1 \exp(-\bar{x}'\sqrt{\bar{\gamma}}) + C_2 \exp(\bar{x}'\sqrt{\bar{\gamma}}). \tag{S.20}$$

Neglecting the growing exponential C_2, the following exponential decay can be predicted

$$\bar{u}_p(\bar{x}') = \frac{2}{\bar{\gamma}}\Big(\bar{\tau}_{k,b} + (\bar{\tau}_{k,0} - \bar{\tau}_{k,b}) \exp(-\bar{x}'\sqrt{\bar{\gamma}})\Big). \tag{S.21}$$

Remembering that in the case of stress barrier $\bar{\tau}_{k,b} < 0$, the equation above has a positive root $\bar{u}_p(\bar{x}' = \bar{L}_{\mathrm{arr}}) = 0$ which can be used to predict the critical barrier length:

$$\bar{L}_{\mathrm{arr}} = \bar{\gamma}^{-\frac{1}{2}} \ln\left(\frac{\bar{\tau}_{k,0} - \bar{\tau}_{k,b}}{-\bar{\tau}_{k,b}}\right). \tag{S.22}$$

Another prediction can be made by searching C_1 and C_2 such that both $\bar{u}_p(\bar{x}')$ and its first derivative are zero at $\bar{x}' = \bar{L}_{\mathrm{arr}}$ and corresponds to:

$$\bar{u}_p(\bar{x}') = \frac{-2\bar{\tau}_{k,b}}{\bar{\gamma}}\Big(\cosh\Big((\bar{x}' - \bar{L}_{\mathrm{arr}})\sqrt{\bar{\gamma}}\Big) - 1\Big). \tag{S.23}$$

In such case, the theoretical prediction of the arrest length becomes

$$\bar{L}_{\mathrm{arr}} = \bar{\gamma}^{-\frac{1}{2}} \mathrm{arccosh}\left(\frac{\bar{\tau}_{k,0} - \bar{\tau}_{k,b}}{-\bar{\tau}_{k,b}}\right). \tag{S.24}$$

The two predictions (S.21) and (S.23) are compared to the the slip profile obtained from numerical simulation in Figure S2.

S.3.2. Slip-weakening friction with $\bar{u}_p \leq \bar{d}_c$

Such case describes frictional weakening which does not reach a residual value. The breakdown work depends on the final slip $\bar{u}_p$

$$\bar{W}_b(\bar{u}_p) = \int_0^{\bar{u}_p} \bar{\tau}_f(\bar{u})\,\mathrm{d}\bar{u} = \int_0^{\bar{u}_p} (1 - \frac{\bar{u}}{\bar{d}_c})\,\mathrm{d}\bar{u} = \bar{u}_p\Big(1 - \frac{\bar{u}_p}{2\bar{d}_c}\Big), \tag{S.25}$$

and leads to a similar pulse equation:

$$\frac{\partial^2 \bar{u}_p}{\partial \bar{x}^2} = \Big(\bar{\gamma} - \frac{1}{\bar{d}_c}\Big)\bar{u}_p - 2(\bar{\tau}_k - 1). \tag{S.26}$$

S.3.3. Slip-weakening friction with $\bar{u}_p > \bar{d}_c$

If one assumes that frictional weakening and associated breakdown work reach constant values ($\bar{W}_b = \bar{d}_c/2$), the pulse equation becomes non-linear:

$$\frac{\partial^2 \bar{u}_p}{\partial \bar{x}^2} = \bar{\gamma}\bar{u}_p - 2\bar{\tau}_k + \frac{\bar{d}_c}{\bar{u}_p}. \tag{S.27}$$

S.3.4. Steady-state energy balance

Thøgersen, Aharonov, Barras, and Renard (2021) derived the steady-state pulse solution for Amontons-Coulomb friction and homogeneous stress condition. The steady-state pulse has a width

$$\bar{\omega} = \pi\sqrt{\frac{\bar{v}_c^2 - 1}{\bar{\gamma}}} = \frac{\pi\bar{\tau}_k}{\sqrt{\bar{\gamma}(1 - \bar{\tau}_k^2)}} \tag{S.28}$$

over which the slip evolves as

$$\bar{u}(\bar{\xi}) = \frac{\bar{\tau}_k}{\bar{\gamma}}\Big(1 - \sin(\pi\bar{\xi}/\bar{\omega})\Big), \tag{S.29}$$

with $\bar{\xi} \in [-\bar{\omega}/2, \bar{\omega}/2]$ being a co-moving frame of reference centered at the position of peak slip velocity. Integrating the steady state solution between $-\bar{\omega}/2$ and $\bar{\omega}/2$ following Eqs. (12) and (13), one can compute the mechanical (reversible) energy stored within the steadily travelling pulse:

$$E_{\text{pulse}} = \frac{1}{2}\int_{-\bar{\omega}/2}^{\bar{\omega}/2}\Big\{\Big(\frac{\partial\bar{u}}{\partial\bar{x}}\Big)^2 + \bar{\gamma}\bar{u}^2 + \Big(\frac{\partial\bar{u}}{\partial\bar{t}}\Big)^2\Big\}d\bar{x} = \frac{\pi\bar{\tau}_k(1+\bar{\tau}_k^2)}{2\bar{\gamma}^{3/2}\sqrt{1-\bar{\tau}_k^2}}. \tag{S.30}$$

S.4. Crack equations

S.4.1. Steady-state solution under homogeneous stress conditions

A crack-like rupture involves different energy transfer than the pulse-like rupture discussed in the previous section. To complement the steady-state pulse solution (S.29) from Thøgersen et al. (2021), we derive hereafter an equivalent self-similar crack solution under homogeneous prestress $\bar{\tau}_k$. Figure S3 presents three different simulations of crack-like rupture ($\Gamma = 0$) under three different homogeneous pre-stress conditions. Under such conditions, the crack reaches constant propagation speed such that, in the co-moving frame $\bar{\zeta} = \bar{x}/\bar{L}$, self-similar profiles are observed for the acceleration $\ddot{\bar{u}}$, the rescaled velocity $\dot{\bar{u}}\bar{t}^{-1}$ and the rescaled displacement $\bar{u}\,\bar{t}^{-2}$. From these results, one can postulate the following self-similar solution:

$$\begin{aligned}
\bar{u} &= \bar{t}^2\mathcal{F}(\bar{\zeta}), && \text{with } \bar{\zeta} = \frac{\bar{x}}{\bar{v}_c\bar{t}},\\
\dot{\bar{u}} &= \bar{t}\mathcal{H}(\bar{\zeta}), && \text{with } \mathcal{H}(\bar{\zeta}) = 2\mathcal{F}(\bar{\zeta}) - \bar{\zeta}\mathcal{F}'(\bar{\zeta}),\\
\ddot{\bar{u}} &= \mathcal{J}(\bar{\zeta}), && \text{with } \mathcal{J}(\bar{\zeta}) = 2\mathcal{F}(\bar{\zeta}) - 2\bar{\zeta}\mathcal{F}'(\bar{\zeta}) + \bar{\zeta}^2\mathcal{F}''(\bar{\zeta}),
\end{aligned} \tag{S.31}$$

where $\mathcal{F}(\bar{\zeta})$ is the self-similar crack displacement solution to be determined. First, this solution needs to satisfy the one-dimensional momentum balance Eq. (1), which becomes in the new frame of reference:

$$2\mathcal{F} - 2\bar{\zeta}\frac{d\mathcal{F}}{d\bar{\zeta}} + (\bar{\zeta}^2 - \frac{1}{\bar{v}_c^2})\frac{d^2\mathcal{F}}{d\bar{\zeta}^2} = \bar{\tau}_k. \tag{S.32}$$

Eq. (S.32) is a Cauchy-Euler equation that reduces to

$$2C - \frac{2A}{\bar{v}_c^2} = \bar{\tau}_k, \tag{S.33}$$

for homogeneous $\bar{\tau}_k$ and if $\mathcal{F}$ has a quadratic form $\mathcal{F} = A\bar{\zeta}^2 + B\bar{\zeta} + C$. A single quadratic solution could not match the simulation profiles, such that the following bi-quadratic solution was postulated:

$$\mathcal{F}(\bar{\zeta}) = \begin{cases} A_1\bar{\zeta}^2 + B_1\bar{\zeta} + C_1, & \text{if } \bar{\zeta} < \bar{\zeta}_c \\ A_2\bar{\zeta}^2 + B_2\bar{\zeta} + C_2, & \text{if } \bar{\zeta} > \bar{\zeta}_c \end{cases} \tag{S.34}$$

Next, the following conditions are imposed

- Zero slip and slip velocity at the fixed boundary on the left of the domain: $\mathcal{F}(\bar{\zeta} = 0) = \mathcal{H}(\bar{\zeta} = 0) = 0$;
- Zero slip and slip velocity at the tip of the crack: $\mathcal{F}(\bar{\zeta} = 1) = \mathcal{H}(\bar{\zeta} = 1) = 0$;
- Continuity of slip and slip velocity at $\bar{\zeta} = \bar{\zeta}_c$;
- The two polynomials should satisfy the momentum balance relationship of Eq. (S.33).

They provide seven conditions to determine the seven unknowns of the self-similar solution which becomes

$$\mathcal{F}(\bar{\zeta}) = \begin{cases} \bar{\tau}_k \bar{v}_c^2 \Big(-\dfrac{1}{2}\bar{\zeta}^2 + \dfrac{\bar{\zeta}}{\bar{v}_c + 1} \Big), & \text{if } \bar{\zeta} < \dfrac{1}{\bar{v}_c} \\ \dfrac{\bar{\tau}_k \bar{v}_c^2}{2(\bar{v}_c^2 - 1)} \Big(\bar{\zeta}^2 - 2\bar{\zeta} + 1 \Big), & \text{if } \bar{\zeta} > \dfrac{1}{\bar{v}_c}. \end{cases} \tag{S.35}$$

Note that $\bar{\zeta}_c = \bar{v}_c^{-1}$ corresponds to the characteristic line $\bar{x} = \bar{t}$ describing the wave speed propagation. The crack solution corresponds then to the combination of a subsonic and a supersonic contribution. For Amontons-Coulomb friction, supersonic rupture speeds are in agreement with the prediction of Amundsen et al. (2015):

$$\bar{v}_c = \frac{1}{\sqrt{1 - \bar{\tau}_k^2}}, \tag{S.36}$$

which is used in Figure S3 to validate the self-similar solution against the different simulations with no free parameter. Next, the crack energy balance can be studied by inserting the self-similar solution of Eq. (S.31) into Eqs. (12), (13), and (14):

$$E_{\rm el} + E_{\rm kin} = W_{\rm ext} \tag{S.37}$$

$$\frac{1}{2}\int_0^{\bar{L}} \left(\frac{\partial \bar{u}}{\partial \bar{x}}\right)^2 d\bar{x} + \frac{1}{2}\int_0^{\bar{L}} \left(\frac{\partial \bar{u}}{\partial \bar{t}}\right)^2 d\bar{x} = \int_0^{\bar{L}} \bar{\tau}_k \bar{u} d\bar{x} \tag{S.38}$$

$$\Leftrightarrow \frac{\bar{t}^3}{2\bar{v}_c}\int_0^1 \Big(\mathcal{F}'(\bar{\zeta})\Big)^2 d\bar{\zeta} + \frac{\bar{t}^3\bar{v}_c}{2}\int_0^1 \Big(\mathcal{H}(\bar{\zeta})\Big)^2 d\bar{\zeta} = t^3\bar{v}_c\bar{\tau}_k\int_0^1 \mathcal{F}(\bar{\zeta})d\bar{\zeta} \tag{S.39}$$

$$\Leftrightarrow \frac{\bar{\tau}_k^2\bar{v}_c^2\bar{t}^3}{6(\bar{v}_c+1)^2} + \frac{\bar{\tau}_k^2\bar{v}_c^3\bar{t}^3}{6(\bar{v}_c+1)^2} = \frac{\bar{\tau}_k^2\bar{v}_c^2\bar{t}^3}{6(\bar{v}_c+1)}. \tag{S.40}$$

Equation (S.40) is satisfied for any rupture speed $\bar{v}_c$ and at any time step $\bar{t}$ and confirms the validity of the self-similar solution of Eq. (S.31). The left-hand side of Eq. (S.40) corresponds to the mechanical energy stored in the crack that can be defined as,

$$\bar{E}_{\rm crack} = \frac{\bar{\tau}_k^2\bar{L}^3}{6\bar{v}_c(\bar{v}_c+1)}, \tag{S.41}$$

which is equivalent to Eq. (S.30) for slip pulse. $\bar{E}_{\rm crack}$ corresponds to the amount of external work that is released by the rupture and converted into internal energy.

As discussed in the main text, $\bar{E}_{\rm crack}$ can be used to derive $\bar{G}$, the fracture mechanics energy release rate (see Eq. (29)). Next, the one-dimensional dynamic fracture energy balance ($\bar{G} = \bar{G}_c$) can be used to define the crack propagation criterion:

$$\bar{d}_c \leq \frac{\bar{\tau}_k^2\bar{x}_b^2}{\bar{v}_c(\bar{v}_c+1)} \equiv \bar{d}_c^0. \tag{S.42}$$

If satisfied, the condition Eq. (S.42) implies that the rupture releases enough energy to advance through the barrier. In practice, $\bar{d}_c^0$ systematically underestimates the fracture energy $\bar{d}_c$ required to arrest the rupture. Indeed, if the condition of Eq. (S.42) is violated, the propagating crack dissipates more energy than it releases such that rupture will arrest once the internal energy available in the 1D system is dissipated. The arrest condition should also account for the length over which the crack stops, such that the crack arrest condition rather writes

$$\bar{d}_c > \frac{\bar{\tau}_k^2(\bar{x}_b + \bar{L}_{\mathrm{arr}})^2}{\bar{v}_c(\bar{v}_c + 1)} \equiv \bar{d}_c^*. \tag{S.43}$$

In the equation above, $\bar{L}_{\mathrm{arr}}$ can be estimated as the ruptured length required for the fracture energy to dissipate the internal energy. Unlike rupture in infinite domain, the energy released by the one-dimensional rupture remains close to the interface and the internal energy is given by $\bar{E}_{\mathrm{crack}}$ defined in Eq. (S.41), such that

$$\bar{L}_{\mathrm{arr}} = \frac{\bar{\tau}_k^2 \bar{x}_b^3}{3\bar{d}_c \bar{v}_c(\bar{v}_c + 1)} \cong \frac{\bar{\tau}_k^2 \bar{x}_b^3}{3\bar{v}_c(\bar{v}_c + 1)} \frac{\bar{v}_c(\bar{v}_c + 1)}{\bar{\tau}_k^2 \bar{x}_b^2} = \frac{1}{3}\bar{x}_b, \tag{S.44}$$

where the last approximation corresponds to $\bar{d}_c \approx \bar{d}_c^0$. Combining equation (S.43) and (S.44) together with the relationship (S.36) between rupture speed and prestress derived by Amundsen et al. (2015), the minimal value of $\bar{d}_c$ required to arrest a steadily propagating crack corresponds then to

$$\bar{d}_c^*(\bar{\tau}_k, \bar{x}_b) = \left(\frac{4\bar{x}_b}{3}\right)^2 (1 - \bar{\tau}_k^2)\left(1 - \sqrt{1 - \bar{\tau}_k^2}\right). \tag{S.45}$$

S.4.2. Linearly decaying pre-stress

In this section, we aim to derive a solution for the final slip observed after the propagation of a crack-like rupture through decaying profile of pre-stress. Both linear decay $\bar{\tau}_k = 1 - \bar{\alpha}\bar{x}$ and quadratic decay $\bar{\tau}_k = 1 - \bar{\lambda}\bar{x}^2$ are discussed. First, we use the crack arrest conditions in absence of fracture energy ($\bar{K}(\bar{L}_{\mathrm{arr}}) = 0$) to predict the arrest position being respectively $\bar{L}_{\mathrm{arr}} = 2/\bar{\alpha}$ and $\bar{L}_{\mathrm{arr}} = \sqrt{3/\bar{\lambda}}$. Next we define the following system of coordinates $\bar{\psi} = \bar{x}/\bar{L}_{\mathrm{arr}}$ and consider the following cubic slip profile $\bar{u}_p(\bar{\psi}) = \mathcal{C}\bar{\psi}(1 - \bar{\psi})^2$, which is defined to satisfy the no-slip boundary condition ($\bar{u}_p(0) = 0$) as well as zero slip ($\bar{u}_p(1) = 0$) and zero longitudinal stress ($\partial \bar{u}_p(1)/\partial \bar{\psi} = 0$) at the arrest position. The remaining constant $\mathcal{C}$ is set such that $\bar{u}_p$ satisfies the crack energy balance, which implies that the elastic strain energy present in the system after the rupture

$$\bar{E}_{\text{el}} = \frac{1}{2}\int_0^1 \left(\frac{\partial \bar{u}_p}{\partial \bar{\psi}}\right)^2 \bar{L}_{\text{arr}}^{-1}\,\mathrm{d}\bar{\psi} = \begin{cases} \dfrac{\bar{\alpha}}{30}\mathcal{C}^2 \\ \sqrt{\dfrac{\bar{\lambda}}{3}}\dfrac{\mathcal{C}^2}{15} \end{cases} \tag{S.46}$$

corresponds to the work injected in the system by the external forces during the rupture

$$\bar{W}_{\text{ext}} = \int_0^1 \bar{\tau}_k(\psi)\bar{u}_p(\psi)\bar{L}_{\text{arr}}\,\mathrm{d}\bar{\psi} = \begin{cases} \bar{\alpha}^{-1}\dfrac{\mathcal{C}}{30} \\ \sqrt{\dfrac{3}{\bar{\lambda}}}\dfrac{\mathcal{C}}{30} \end{cases} \tag{S.47}$$

The rupture energy balance leads then to respectively $\mathcal{C} = \bar{\alpha}^{-2}$ and $\mathcal{C} = 1.5\bar{\lambda}^{-1}$ and the following slip profile

$$\frac{\bar{u}_p(\bar{\psi})}{\bar{u}_p^*} = \frac{27\psi}{4}(1-\psi)^2, \tag{S.48}$$

with the peak value of frictional slip corresponding respectively to $\bar{u}_p^* = 4\bar{\alpha}^{-2}/27$ and $\bar{u}_p^* = 2\bar{\lambda}^{-1}/9$ and being observed at one third of the total rupture length ($\bar{\psi}_{\max} = 1/3$). The solution (S.48) is shown by the white dashed line in Fig. 8 in comparison with simulations.

S.5. Connection with existing linear elastic fracture mechanics models

Linear elastic fracture mechanics provides an elegant and robust framework to describe the arrest of frictional rupture in lab experiments. The *small-scale yielding* assumption behind linear elastic fracture theory implies that the material behavior is everywhere linear elastic, apart from a region near the fracture tip which is of negligible size compared to any other representative length scale of the problem. The most frequent boundary conditions assumed unbounded elastic domain under constant stress, which allows for expressing the crack arrest criterion as function of the energy released at the tip of the crack per unit crack surface growth:

$$G \sim \frac{K^2}{2\mathcal{G}}. \tag{S.49}$$

G is often referred to as the *energy release rate* and is function of the stress intensity factor K that characterises the amplitude of the stress concentration near the crack tip. For example, the stress intensity factor of a mode-II crack of size L at the edge of a semi-infinite domain is given by the integration of the pre-stress (Kammer et al., 2015):

$$K(L) = \frac{2}{\sqrt{\pi L}} \int_0^L \frac{(\tau_0 - \mu_k \sigma_n)\mathcal{M}(\xi/L)}{\sqrt{1-(\xi/L)^2}}\, \mathrm{d}\xi, \tag{S.50}$$

with $\mathcal{M}(\xi/L) = 1 + 0.3(1-(\xi/L)^{5/4})$. Using the two equations above, crack arrest is predicted as soon as the fracture energy of the interface exceeds the energy release rate:

$$G(L) \leq G_c. \tag{S.51}$$

Such dynamics is similar to the one predicted in the one-dimensional domain under stress-controlled boundary conditions. Two notable differences arise from the small-H approximation. First, the energy release rate scales as $\bar{G} \sim \bar{L}^2$ (see Eq.(29)) whereas it scales as $G \sim L$ in the unbounded domain approximation. This difference is caused by the introduction of an additional characteristic length scale (H) in the one-dimensional system. The same quadratic scaling is also observed in the energy release rate controlling the tensile delamination of double cantilever beam with similarly large aspect ratio (Anderson, 2005). Second, the tip singularity is regularized over the thickness H in the one-dimensional model, such that $\bar{K}$ does not describe the stress singularity, but rather the resultant stress at the tip, as evident in the integration of $\bar{K}(\bar{L})$ in Eq. (27), the one-dimensional equivalent of Eq. (S.50).

Another useful type of boundary conditions assumes rupture propagating between two thin-strips loaded by an imposed-displacement at the boundary (Marder, 1998; Weng &

Ampuero, 2019). In such geometry, the energy release rate rather writes:

$$G_0 = \frac{(\tau_0 - \mu_k \sigma_n)^2 H}{\mathcal{G}}. \tag{S.52}$$

Assuming small acceleration, Marder (1998) derives an approximate equation of motion for linear elastic tensile fracture in the thin-strip setup, which was recently adapted to frictional rupture by Weng and Ampuero (2019):

$$G_c = G_0\Big(1 - \frac{\dot{v}_r H}{\mathcal{A}(v_r)}\Big), \tag{S.53}$$

with v_r being the rupture speed and $\mathcal{A}$ a positive function of v_r. An important difference is that ruptures in the thin-strip geometry are pulse-like, whereas crack-like ruptures are promoted in the unbounded elastic domain. Another difference with the unbounded configuration described in Eq. (S.51) is that the thin-strip introduces some inertia in the crack equation of motion in Eq. (S.53) that stretches the arrest of the rupture over some finite arrest length. Such configuration is then equivalent to the displacement-controlled boundary conditions of the one-dimensional model. Whereas the analogy between unbounded domain and one-dimensional stressed-controlled setup was qualitative, the one-dimensional model under displacement-controlled boundary conditions directly describes the thin-strip geometry and the analogy is quantitative. For example, both in Eq. (S.53) and Eq. (21), the rupture will decelerate and ultimately arrest if

$$\frac{(\tau_0 - \mu_k \sigma_n)^2 H}{\mathcal{G}} \leq G_c. \tag{S.54}$$

Moreover, the predictions of the two models show a similar trend in the limit $\bar{d}_c \to \bar{d}_c^*$. Figure S4 compares the arrest length of one-dimensional simulations discussed in Fig. 5B of this paper to the following approximation proposed in the equation (22) of Weng and Ampuero (2019) to describe the rupture arrest observed in 2.5-dimensional earthquake simulations, which can be written in our dimensionless formulation as:

$$\bar{L}_{\mathrm{arr}} = \frac{\alpha_s^{-0.6} - 1}{0.72(\bar{d}_c/\bar{d}_c^* - 1)}, \tag{S.55}$$

with $\alpha_s = \sqrt{1 - \bar{v}_c^2}$ defined for subsonic rupture velocity in two- and three-dimensions elastodynamics. As discussed by (Amundsen et al., 2015), one-dimensional elastodynamics promotes rupture speed which are faster than the one-dimensional wave speed (see Eq. (S.36)), which explains the large value ($\bar{v}_c = 0.975$) that should be used in Eq. (S.55) to describe the one-dimensional simulations in Fig. S4. For large $\bar{d}_c \to \bar{d}_c^*$, the small-scale yielding assumption is no longer valid such that linear elastic fracture mechanics prediction does not capture the plateau observed with the one-dimensional model.

S.6. Seismic data from 2019 Ridgecrest M_w7.1 earthquake

The data plotted in the panel (c) of Figure 9 are computed from the surface fault slip caused by the M_w7.1 Ridgecrest earthquake and inverted from optical image correlation by Chen et al. (2020). First, the strike parallel slip profile inverted from images of Sentinel-1 shown in the figure 2c of Chen et al. (2020) are digitized. Next, the non-dimensional variables $\bar{u}_p$ and $\bar{x}$ are computed respectively from the slip and the distance along strike using Table S1 (mode-II column) and assuming the following parameters: $H = 1$ [km], $\sigma_n = 200$ [MPa], $(\mu_s - \mu_k) = 0.7$ [-], $\mathcal{G} = 35$ [GPa] and the Poisson's ratio $\nu = 0.25$ [-]. As shown in Figure S5, $\bar{u}_p(\bar{x})$ is then interpolated by a cubic spline used to evaluate its second derivative and to compute $\bar{\tau}_k$ from the pulse equation Eq. (33) with ð set as 2 (negligible fracture energy).

S.7. Stress drop and back-propagating front with displacement-controlled boundary conditions ($\Gamma = 1$)

The displacement field along the interface before $\bar{u} = 0$ and after $\bar{u} = \bar{u}_p$ should satisfy the momentum equation (1) with zero acceleration. Before the rupture, this static equilibrium implies that the dimensionless stress $\bar{\tau} = 0$, which means that the frictional stress at the interface equates the initial stress in the bulk ($\bar{\tau}_f = \bar{\tau}_k$). After the rupture, the dimensionless stress becomes

$$\bar{\tau} = \bar{\tau}_k - \bar{\tau}_f = \bar{\gamma}\bar{u}_p - \frac{\partial^2 \bar{u}_p}{\partial \bar{x}^2}. \tag{S.56}$$

Moreover, one knows that the final slip should approximately satisfy the pulse equation (33), which implies that

$$\bar{\gamma}\bar{u}_p - \frac{\partial^2 \bar{u}_p}{\partial \bar{x}^2} = \eth\bar{\tau}_k. \tag{S.57}$$

Combining Eqs. (S.56-S.57), one obtains that the frictional stress at the interface after the rupture corresponds to $\bar{\tau}_f = (1 - \eth)\bar{\tau}_k$, which leads to the following stress drop:

$$\Delta\bar{\tau}_f = \eth\bar{\tau}_k. \tag{S.58}$$

For the largest admissible fracture energy (i.e. $\bar{d}_c = \bar{d}_c^*$ and therefore $\eth = 1$), the stress drop corresponds to $\Delta\bar{\tau}_f = \bar{\tau}_k$, which means that the rupture completely releases the initial shear stress ($\bar{\tau}_f = 0$). Conversely, for negligible fracture energy, $\eth = 2$ and the frictional stress after failure becomes $\bar{\tau}_f = -\bar{\tau}_k$. In dimensional unit, such overshoot can inverse the sign of the shear loading at the interface after the rupture.

If at the end of the rupture, the interface is strained with negative shear stress, it can host a secondary rupture with reverse (i.e. negative) slip and slip velocity. The same 1D pulse theory can be used to describe the propagation of this reverse secondary rupture.

First, one need to define the negative pre-stress, the equivalent of Eq.(3) but for negative slip velocity:

$$\bar{\tau}_k^-(\bar{x}) = \frac{\tau_0(\bar{x})/\sigma_n + \mu_k}{\mu_s - \mu_k} = \bar{\tau}_k(\bar{x}) + \frac{2\mu_k}{\mu_s - \mu_k} \equiv \bar{\tau}_k(\bar{x}) + \bar{\vartheta}. \tag{S.59}$$

Second, one defines the displacement due to the secondary rupture front only, $\bar{u}^- = -(\bar{u} - \bar{u}_p)$, where the minus sign is there to ensure that $\bar{u}^- > 0$. With this two ingredients, the momentum equation within the secondary rupture writes:

$$-\ddot{\bar{u}}^- = \frac{\partial^2(\bar{u}_p - \bar{u}^-)}{\partial \bar{x}^2} - \bar{\gamma}(\bar{u}_p - \bar{u}^-) + \tau_k^-, \tag{S.60}$$

which can be further simplified using Eqs. (S.57) and (S.59) into

$$\ddot{\bar{u}}^- = \frac{\partial^2 \bar{u}^-}{\partial \bar{x}^2} - \bar{\gamma}\bar{u}^- + (\eth - 1)\bar{\tau}_k - \bar{\vartheta}. \tag{S.61}$$

In the equation above both $\bar{u}^-$ and $\ddot{\bar{u}}^-$ are positive such that the theory developed in this paper to describe slip pulse can be applied to describe the dynamics of secondary slip fronts governed by Eq. (S.61). From the original one-dimensional momentum equation (1), frictional rupture are possible if $\bar{\tau}_k = 0$. Similarly, using the updated momentum equation above (S.61), secondary rupture front are possible if:

$$\bar{\tau}_k(\eth - 1) - \bar{\vartheta} > 0. \tag{S.62}$$

The equation above only guarantees that the rupture is energetically admissible. As discussed for Eq. (8), the criterion (S.62) is a necessary condition for back-propagating rupture but is not sufficient. To observe secondary rupture fronts, a local stress concentration is also required to trigger nucleation and typically arises once the main front is arrested by a sharp barrier. Figure S6 shows examples of secondary fronts nucleating at the location of a stress barrier and propagating backward following the prediction of Eq. (S.62).

References

Amundsen, D. S., Scheibert, J., Thøgersen, K., Trømborg, J., & Malthe-Sørenssen, A. (2012). 1D Model of Precursors to Frictional Stick-Slip Motion Allowing for Robust Comparison with Experiments. *Tribology Letters*, *45*(2), 357–369. doi: 10.1007/s11249-011-9894-3

Amundsen, D. S., Trømborg, J. K., Thøgersen, K., Katzav, E., Malthe-Sørenssen, A., & Scheibert, J. (2015). Steady-state propagation speed of rupture fronts along one-dimensional frictional interfaces. *Physical Review E*, *92*(3), 032406.

Anderson, T. L. (2005). *Fracture mechanics: Fundamentals and applications* (3rd ed. ed.). Boca Raton, FL: Taylor & Francis.

Bar-Sinai, Y., Spatschek, R., Brener, E. A., & Bouchbinder, E. (2013). Instabilities at frictional interfaces: Creep patches, nucleation, and rupture fronts. *Phys. Rev. E*, *88*, 060403. Retrieved from `https://link.aps.org/doi/10.1103/PhysRevE.88.060403` doi: 10.1103/PhysRevE.88.060403

Bouchbinder, E., Brener, E. A., Barel, I., & Urbakh, M. (2011). Slow cracklike dynamics at the onset of frictional sliding. *Phys. Rev. Lett.*, *107*, 235501. Retrieved from `https://link.aps.org/doi/10.1103/PhysRevLett.107.235501` doi: 10.1103/PhysRevLett.107.235501

Chen, K., Avouac, J.-P., Aati, S., Milliner, C., Zheng, F., & Shi, C. (2020, January). Cascading and pulse-like ruptures during the 2019 Ridgecrest earthquakes in the Eastern California Shear Zone. *Nature Communications*, *11*(1), 22. doi: 10.1038/s41467-019-13750-w

Courant, R., Friedrichs, K., & Lewy, H. (1928). über die partiellen Differenzengleichungen der mathematischen Physik. *Mathematische annalen*, *100*(1), 32–74.

Cromer, A. (1981). Stable solutions using the Euler approximation. *American Journal of Physics*, *49*(5), 455–459. doi: 10.1119/1.12478

Kammer, D. S., Radiguet, M., Ampuero, J.-P., & Molinari, J.-F. (2015). Linear Elastic Fracture Mechanics Predicts the Propagation Distance of Frictional Slip. *Tribology Letters*, *57*(3), 23. doi: 10.1007/s11249-014-0451-8

Knopoff, L., & Ni, X. X. (2001). Numerical Instability at the Edge of a Dynamic Fracture. *Geophysical Journal International*, *147*(3), 1–6. doi: 10.1046/j.1365-246x.2001.01567.x

Marder, M. (1998). Adiabatic equation for cracks. *Philosophical Magazine B*, *78*(2), 203–214. doi: 10.1080/13642819808202942

Thøgersen, K., Aharonov, E., Barras, F., & Renard, F. (2021). Minimal model for the onset of slip pulses in frictional rupture. *Physical Review E*, *103*(5), 052802. doi: 10.1103/PhysRevE.103.052802

Weng, H., & Ampuero, J.-P. (2019). The Dynamics of Elongated Earthquake Ruptures. *Journal of Geophysical Research: Solid Earth*, *124*(8), 8584–8610. doi: 10.1029/2019JB017684

Physical quantities	Variables	Mode II rupture	Mode III rupture
Characteristic wave speed	$c = \sqrt{\frac{\Lambda}{\rho}}$	$\sqrt{\frac{\lambda + 2\mathcal{G}}{\rho}}$	$\sqrt{\frac{\mathcal{G}}{\rho}}$
Characteristic displacement	$U = H\sigma_n \frac{\mu_s - \mu_k}{\Lambda}$	$H\sigma_n \frac{\mu_s - \mu_k}{\lambda + 2\mathcal{G}}$	$H\sigma_n \frac{\mu_s - \mu_k}{\mathcal{G}}$
Characteristic time	$T = \sqrt{\frac{H^2\rho}{\Lambda}}$	$\sqrt{\frac{H^2\rho}{\lambda + 2\mathcal{G}}}$	$\sqrt{\frac{H^2\rho}{\mathcal{G}}}$
Dimensionless distance	$\bar{x}$	$x\frac{1}{H}$	$x\frac{1}{H}$
Dimensionless displacement	$\bar{u} = \frac{\langle u_i \rangle_y}{U}$	$\frac{\langle u_x \rangle_y}{U}$	$\frac{\langle u_z \rangle_y}{U}$
Dimensionless shear stress	$\bar{\tau} = \frac{T^2}{\rho U H}(\tau_0 - \tau_f)$	$\frac{\sigma_{xy}^0/\sigma_n - \tau_f/\sigma_n}{\mu_s - \mu_k}$	$\frac{\sigma_{yz}^0/\sigma_n - \tau_f/\sigma_n}{\mu_s - \mu_k}$
Dimensionless stiffness	$\bar{\gamma} = \frac{2\mathcal{G}}{\Lambda}$	$\frac{2\mathcal{G}}{\lambda + 2\mathcal{G}}$	2

Table S1. Summary of the non-dimensionalization procedure used in the present study. The elastic parameter Λ is equal to $\lambda + 2\mathcal{G}$ for Mode II rupture, and $\mathcal{G}$ for Mode III rupture.

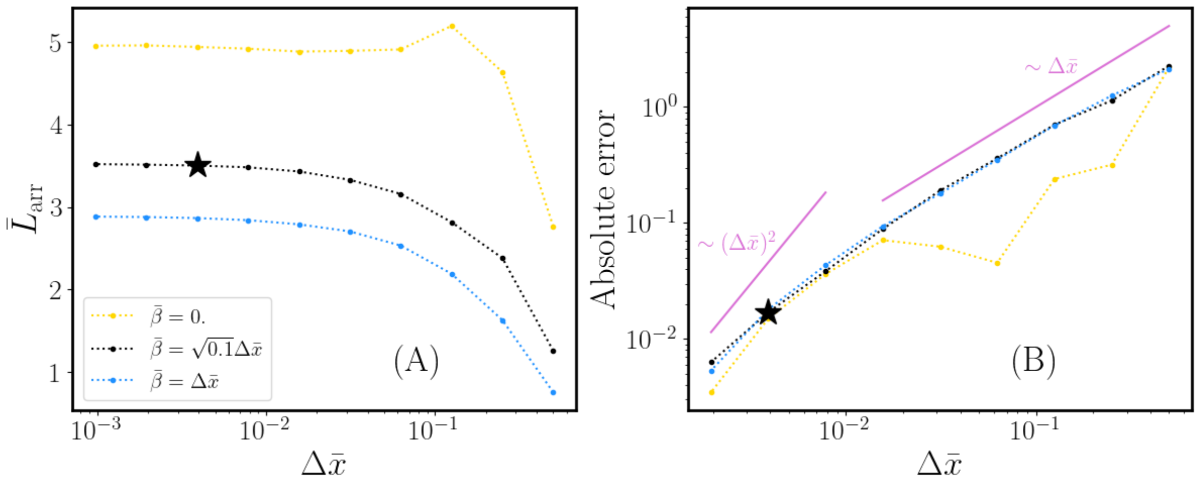

Figure S1. Convergence study of the arrest length $\bar{L}_{arr}$ for a pulse like rupture stopped by a stress barrier with $\tau_{k,0} = 0.6$ and $\tau_{k,b} = -0.3$. The black stars show the set of parameters chosen in this paper. (A) Simulated arrest length for different mesh sizes $\Delta\bar{x}$ and damping parameter $\bar{\beta}$. (B) Evolution of the absolute error (using $\bar{L}_{arr}$ for $\Delta\bar{x} = 10^{-3}$ as the reference value of each case). The purple curves show linear and quadratic convergence rates.

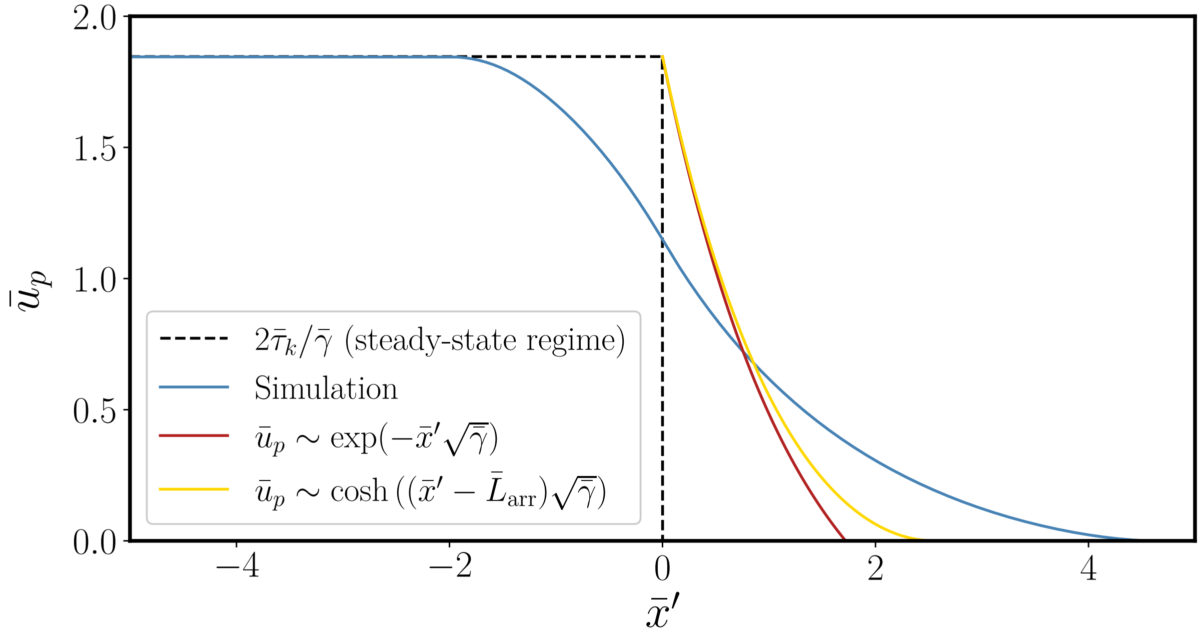

Figure S2. Decay of the final slip observed when a pulse-like rupture is arrested by a stress barrier. The simulation (blue line) is compared to two theoretical predictions derived from the pulse arrest equation (17). The red and yellow curves correspond respectively to Eq. (S.21) and (S.23).

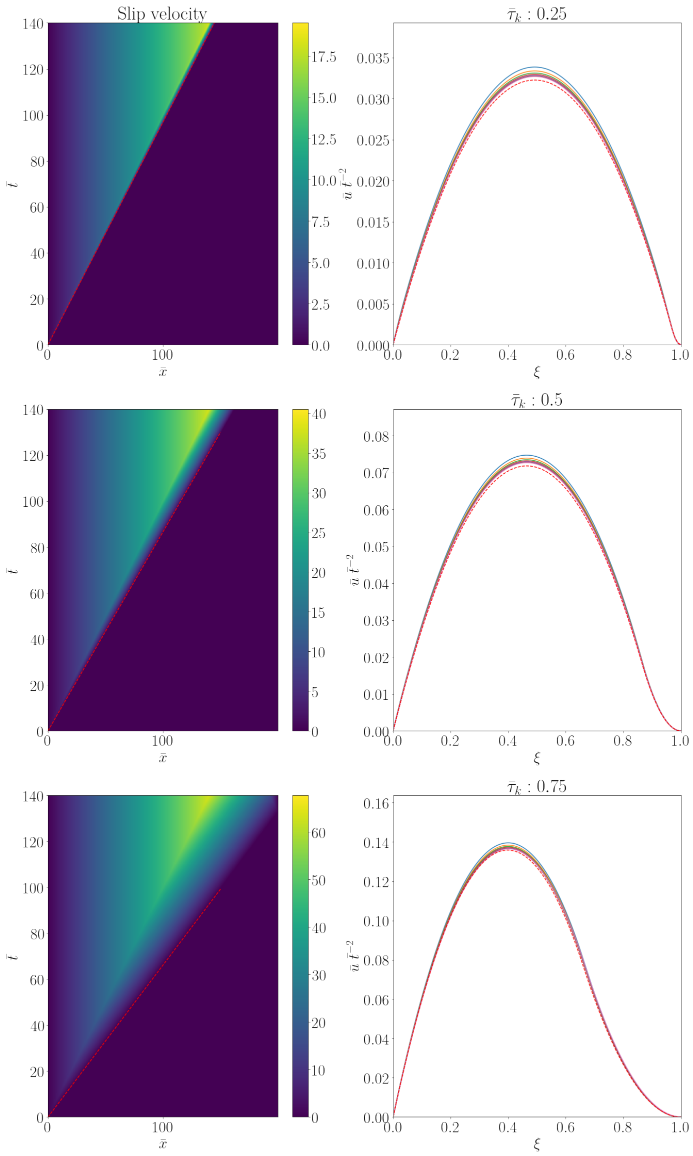

Figure S3. The three rows correspond to crack-like ruptures under three different homogeneous pre-stress $\bar{\tau}_k$ of 0.25, 0.5, and 0.75 from top to bottom. Space-time maps of the rupture are shown on the left column, with the red dashed line highlighting the steady state velocity $\bar{v}_c$ used in the theoretical predictions. The color coding shows the slip velocity. In the right column, the associated slip profile along the interface is shown at different time steps by the solid lines. Curves are collapsed by using the spatial coordinates $\bar{\zeta}$ and rescaling the slip by $\bar{t}^2$. The red dashed lines show the self-similar solution $\bar{u} = t^2\mathcal{F}(\bar{\zeta})$ according to Eq. (S.35) with no adjustable parameter.

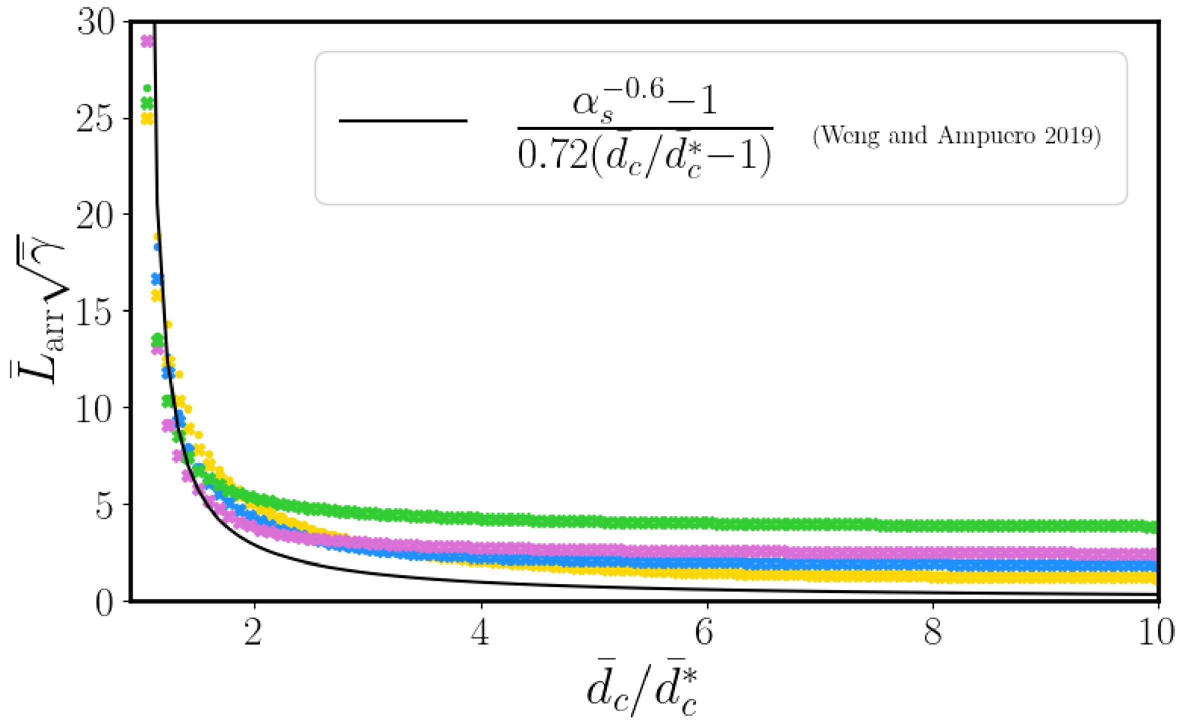

Figure S4. Evolution of the arrest length for pulse-like ruptures that arrest on a fracture energy barrier. The colored data are identical to the one displayed in Fig. 5B. The black line shows the prediction of Weng and Ampuero (2019) using Eq. (S.55) and $\bar{v}_c = 0.975$.

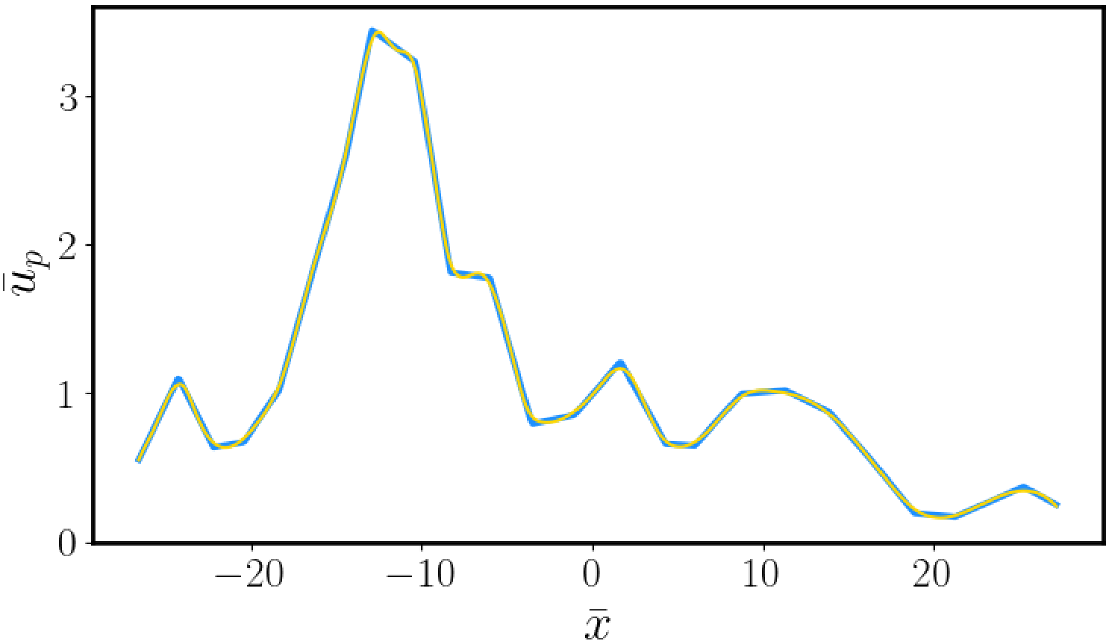

Figure S5. Dimensionless slip versus distance along the fault used to generate Fig. 9c. The blue curve shows the raw data digitized from the figure 2c of Chen et al. (2020) after non-dimensionalization. The yellow curve shows the cubic spline interpolation used to evaluate the second-order derivative of $\bar{u}_p$.

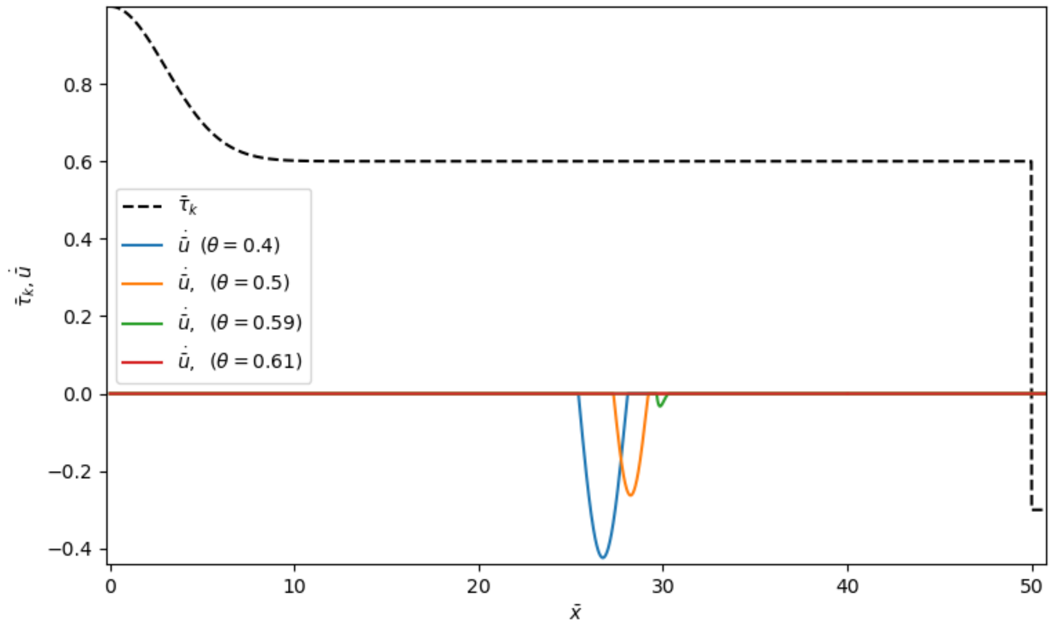

Figure S6. Secondary rupture fronts causing negative slip and propagating from the arresting barrier towards the hypocenter (a.k.a. back-propagating fronts). Snapshot are all taken at the same time step after the arrest of the main rupture front by a stress barrier. The same background stress (black dashed line) is used for the four simulations and corresponds to $\bar{\tau}_k = 0.6$ as well as $\bar{d}_c = 0$. The colored lines show the slip velocity profiles observed at the same time step after the arrest of the main front for different values of $\bar{\vartheta}$. As predicted by Eq. (S.62), back propagating fronts nucleate when $\bar{\tau}_k > \bar{\vartheta}$.